



Long-range angular correlations of charged particles in high multiplicity e^+e^- collisions using archived data from the ALEPH detector at LEP

Anthony Badea, Austin Baty, Gian Michele Innocenti, Yen-Jie Lee,
Christopher McGinn, Bibek Pandit, Michael Peters, and Jesse Thaler

Massachusetts Institute of Technology

Paoti Chang and Tzu-An Sheng

National Taiwan University

Marcello Maggi

Universita degli Studi di Bari

(Dated: February 16, 2018)

Abstract

First results on two-particle angular correlations for charged particles emitted in e^+e^- collisions using $730\ pb^{-1}$ of data collected between 91 and 209 GeV with the ALEPH detector at LEP are presented. With the archived data, the correlation functions are studied over a broad range of pseudorapidity η (rapidity y) and azimuthal angle ϕ with respect to the electron-positron beam axis, the event thrust axis and a dijet axis. Short-range correlations in $\Delta\eta$ (Δy), which are studied with e^+e^- annihilations which reveal jet-like correlations. Long-range azimuthal correlations are studied differentially as a function of charged particle multiplicity. Those results are compared to event generators and are complementary to the particle correlation analyses in high multiplicity proton-proton, proton-nucleus and nucleus-nucleus collisions at the RHIC and the LHC.

I. INTRODUCTION

This analysis note presents the measurements of two-particle angular correlations of charged hadrons produced in e^+e^- collisions as a function of charged hadron multiplicity, using $730\ pb^{-1}$ of archived data collected between 91 and 209 GeV with the ALEPH detector at LEP. Two-particle correlations in high-energy collisions provide valuable information for characterizing Quantum Chromodynamics and have been studied previously for a broad range of collision energies in proton-proton (pp) [?], proton-nucleus (pA) [? ? ?], and nucleus-nucleus (AA) [? ?] collisions. Such measurements can elucidate the underlying mechanism of particle production and reveal possible collective effects resulting from the high particle densities accessible in these collisions.

Studies of two-particle angular correlations in pp, pA and AA collisions are typically performed using two-dimensional $\Delta\eta - \Delta\phi$ correlation functions, where $\Delta\phi$ is the difference in the azimuthal angle ϕ between the two particles and $\Delta\eta$ is the difference in pseudorapidity $\eta = -\ln(\tan(\theta/2))$. The polar angle θ is defined relative to the counterclockwise hadron beam direction.

Of particular interest in studies of collective effects is the long-range (large $|\Delta\eta|$) structure of the two-particle correlation functions. In this region, the function is less susceptible to other known sources of correlations such as resonance decays and fragmentation function of energetic jets. Measurements in high-energy AA collisions have shown significant modification of the long-range structure compared with minimum-bias pp collisions, over a very wide range of collision energies [? ? ? ?]. The long-range correlations are commonly interpreted as a consequence of the hydrodynamical flow of the produced strongly interacting medium [?] and usually characterized by the Fourier components of the azimuthal particle distributions. The extraction of the second and third Fourier components, usually referred to as elliptic and triangular flow, is of great interest because it is closely related to initial collision geometry and its fluctuation [?]. Those measurements allow the extraction of the fundamental transport properties of the medium using hydrodynamic models.

Recently, measurements in pp [?] and pPb collisions [? ? ?] have revealed the emergence of long-range, near-side ($\Delta\phi \sim 0$) correlations in the selection of collisions with very high number of final state particles. This “ridge-like” correlation has inspired a large variety of theoretical models [? ?]. The physical origin of the phenomenon is not yet fully

understood. Moreover, it was found that the elliptic flow signal exists even at the lowest nucleon-nucleon center-of-mass energy of 7.7 GeV in AA collisions at the Relativistic Heavy Ion Collider [?].

Due to the complexity of the hadron-hadron collisions, possible initial state correlations of the partons, such as those arise from color-glass condensate [? ?], could complicate the interpretation of the pp and pA data. Studies of high multiplicity e^+e^- collision, where the initial kinematics of the collisions are well-controlled, could bring significant insights about the observed phenomenon. These measurements will also enable a direct comparison between different collision systems for the first time. The studies of ridge signal in e^+e^- collisions will bring significant impact to the field of relativistic heavy ion collisions, either change completely the interpretation of the ridge in pp, pA and AA collisions if a significant signal is observed, or serve as an important reference for the final state effect observed in high multiplicity hadron-hadron scatterings if no long-range correlation signal was detected.

With the archived data from ALEPH collaboration, the correlation functions are studied over a broad range of pseudorapidity η (rapidity y) and azimuthal angle ϕ with respect to the electron-positron beam axis. In addition, the correlation functions are also studied using azimuthal and polar angles calculated with respect to the event thrust axis and a dijet axis in order to follow the direction of the extending color strings.

II. DATA SAMPLE

Document the ALEPH data used in this analysis

III. DATA QUALITY CHECKS

Basic data quality checks for LEP1, LEP2, and PYTHIA8. The spike in the LEP1 and LEP2 pt spectra near 45 GeV is produced by the particles that took the full beam energy in the transverse plane. The beam energy is 92 GeV so in a two particle configuration each particle will take half of the total energy to conserve various kinematics.

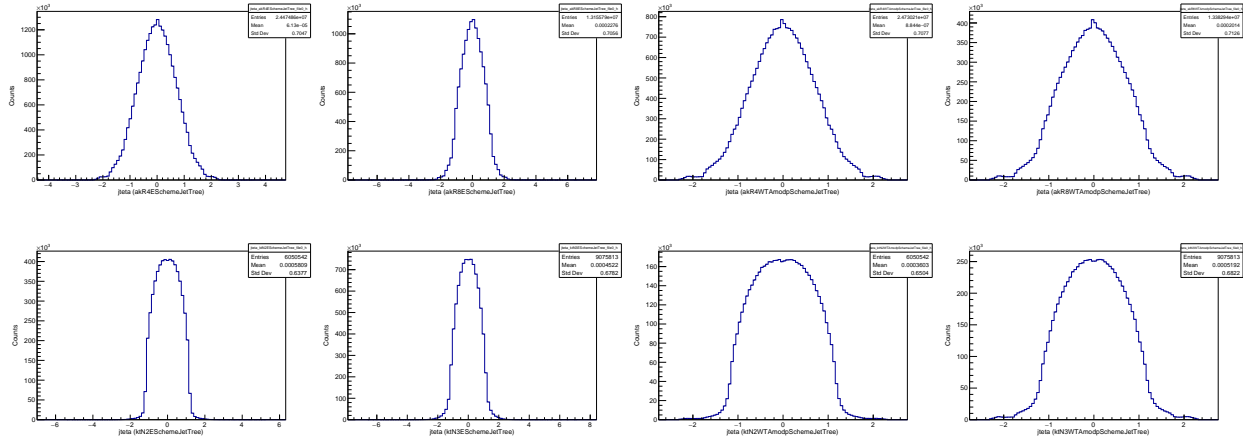


FIG. 1: LEP1 Jet η distributions. Top row: anti- k_t , left to right: $R = 0.4$, E scheme; $R = 0.8$, E scheme; $R = 0.4$, WTA mod p scheme; $R = 0.8$, WTA mod p scheme. Bottom row: k_t , left to right: $N = 2$, E scheme; $N = 3$, E scheme; $N = 2$, WTA mod p scheme; $N = 3$; WTA mod p scheme.

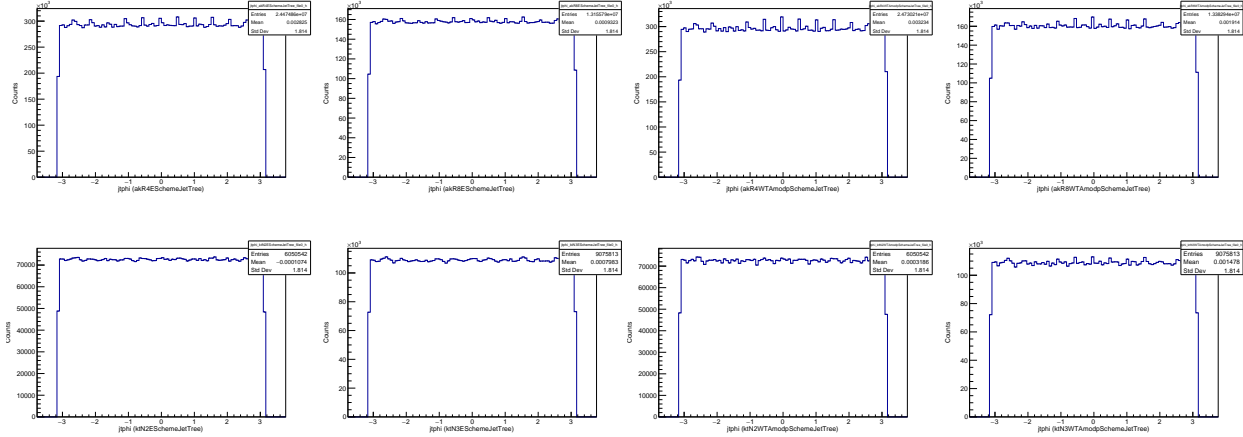


FIG. 2: LEP1 Jet ϕ distributions. Top row: anti- k_t , left to right: $R = 0.4$, E scheme; $R = 0.8$, E scheme; $R = 0.4$, WTA mod p scheme; $R = 0.8$, WTA mod p scheme. Bottom row: k_t , left to right: $N = 2$, E scheme; $N = 3$, E scheme; $N = 2$, WTA mod p scheme; $N = 3$; WTA mod p scheme.

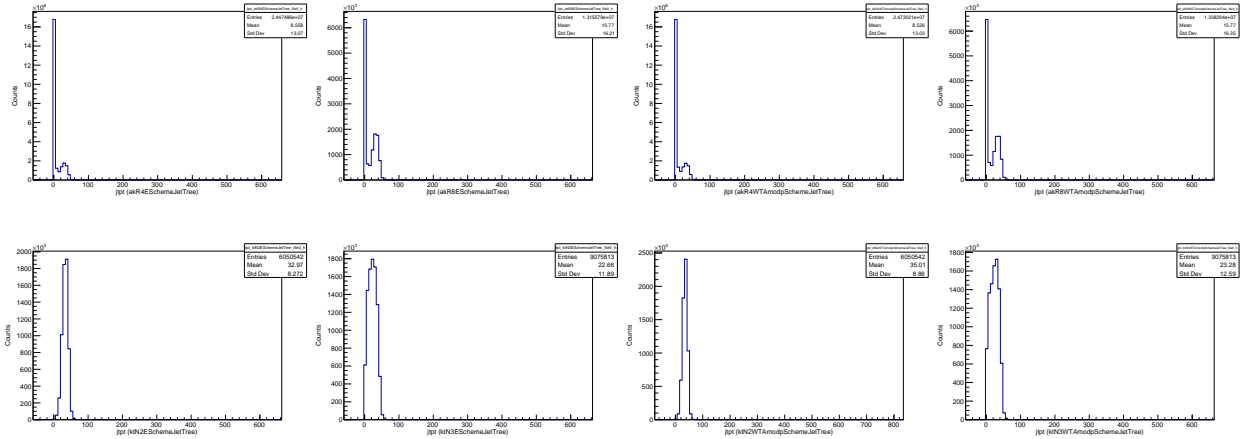


FIG. 3: LEP1 Jet p_t distributions. Top row: anti- k_t , left to right: $R = 0.4, E$ scheme; $R = 0.8, E$ scheme; $R = 0.4, \text{WTA mod p}$ scheme; $R = 0.8, \text{WTA mod p}$ scheme. Bottom row: k_t , left to right: $N = 2, E$ scheme; $N = 3, E$ scheme; $N = 2, \text{WTA mod p}$ scheme; $N = 3; \text{WTA mod p}$ scheme.

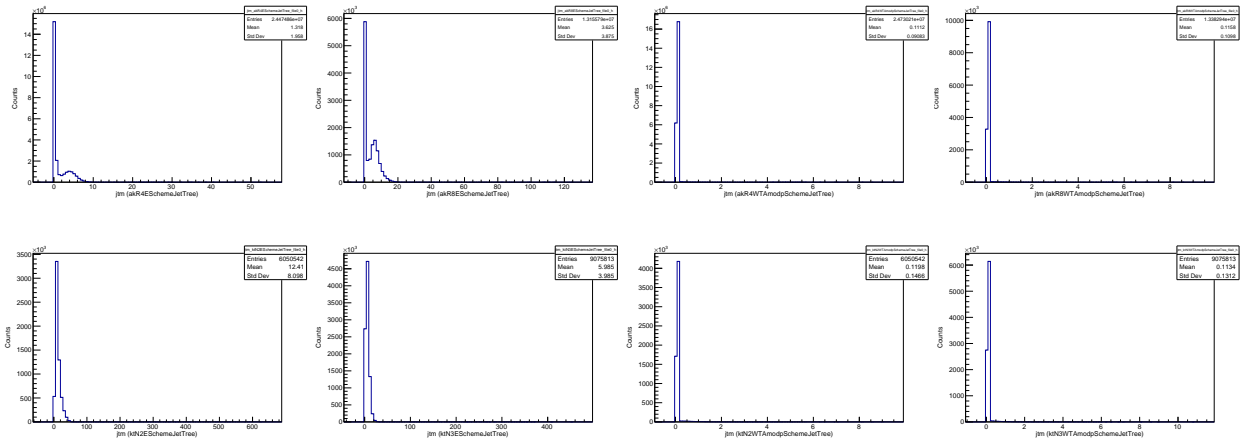


FIG. 4: LEP1 Jet mass distributions. Top row: anti- k_t , left to right: $R = 0.4, E$ scheme; $R = 0.8, E$ scheme; $R = 0.4, \text{WTA mod p}$ scheme; $R = 0.8, \text{WTA mod p}$ scheme. Bottom row: k_t , left to right: $N = 2, E$ scheme; $N = 3, E$ scheme; $N = 2, \text{WTA mod p}$ scheme; $N = 3; \text{WTA mod p}$ scheme.

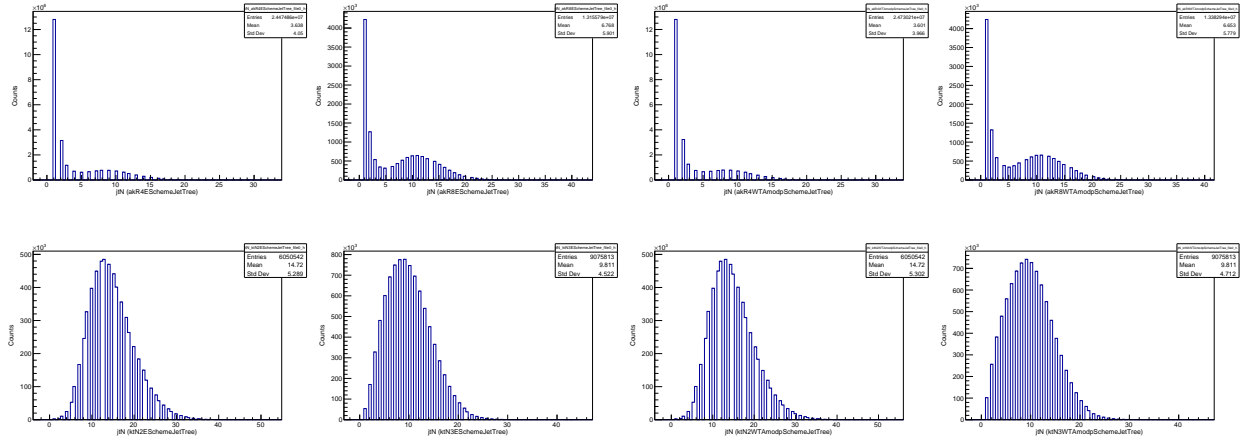


FIG. 5: LEP1 Jet N distributions. Top row: anti- k_t , left to right: $R = 0.4$, E scheme; $R = 0.8$, E scheme; $R = 0.4$, WTA mod p scheme; $R = 0.8$, WTA mod p scheme. Bottom row: k_t , left to right: $N = 2$, E scheme; $N = 3$, E scheme; $N = 2$, WTA mod p scheme; $N = 3$; WTA mod p scheme.

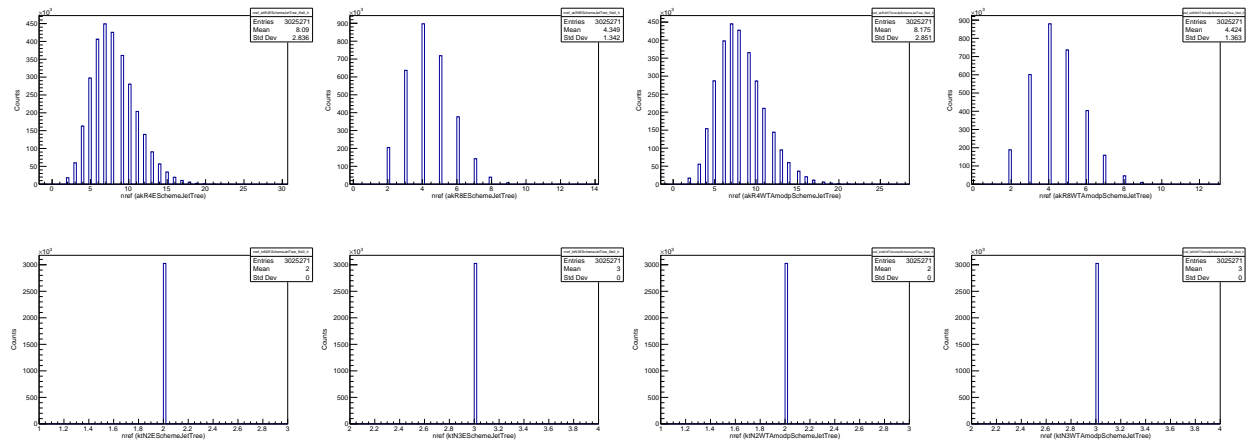


FIG. 6: LEP1 Jet nref distributions. Top row: anti- k_t , left to right: $R = 0.4$, E scheme; $R = 0.8$, E scheme; $R = 0.4$, WTA mod p scheme; $R = 0.8$, WTA mod p scheme. Bottom row: k_t , left to right: $N = 2$, E scheme; $N = 3$, E scheme; $N = 2$, WTA mod p scheme; $N = 3$; WTA mod p scheme.

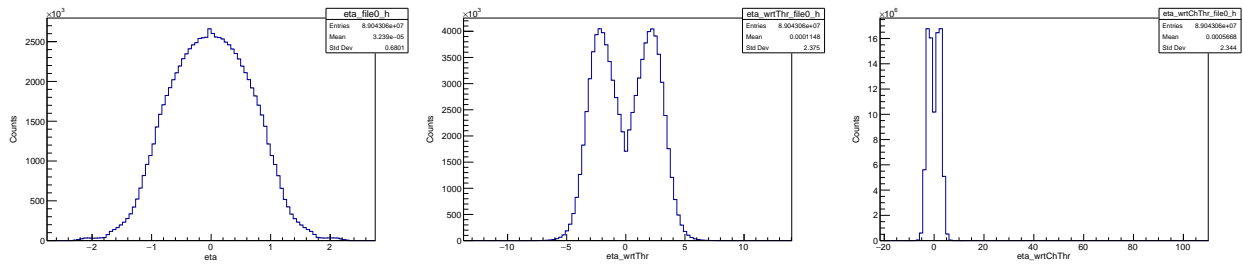


FIG. 7: LEP1 η distributions. Left to right: η ; η with respect to thrust axis; η with respect to charged thrust axis.

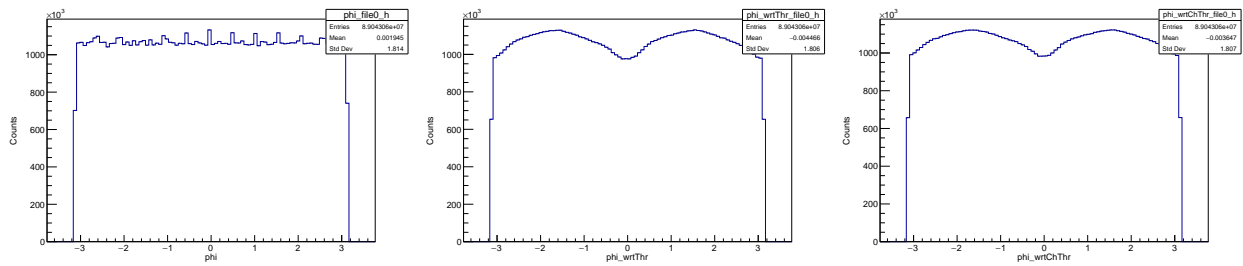


FIG. 8: LEP1 ϕ distributions. Left to right: ϕ ; ϕ with respect to thrust axis; ϕ with respect to charged thrust axis.

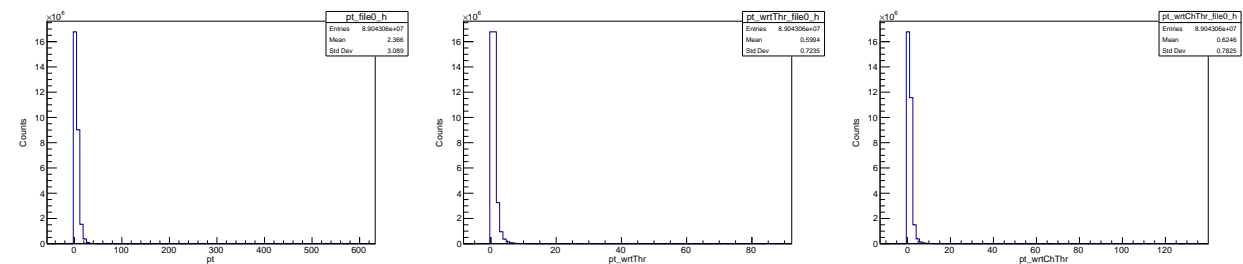


FIG. 9: LEP1 p_t distributions. Left to right: p_t ; p_t with respect to thrust axis; p_t with respect to charged thrust axis.

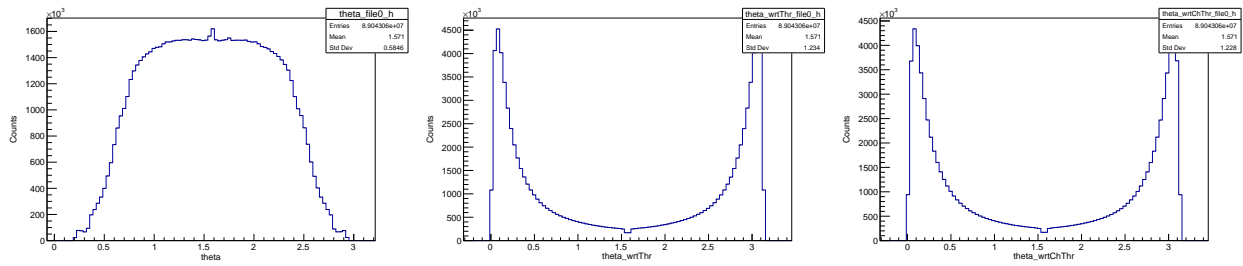


FIG. 10: LEP1 θ distributions. Left to right: θ ; θ with respect to thrust axis; θ with respect to charged thrust axis.

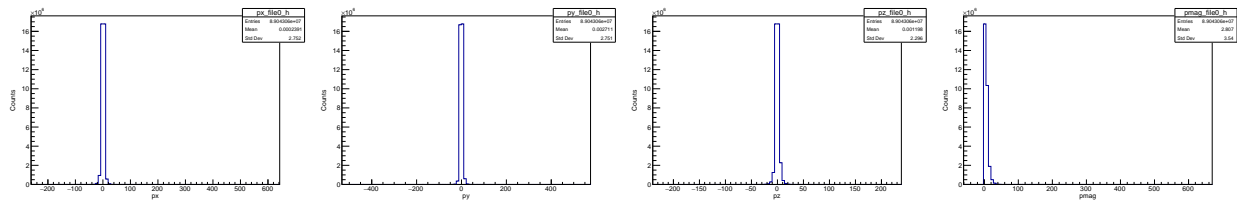


FIG. 11: LEP1 p_x , p_y , p_z , and $|\vec{p}|$ distributions.

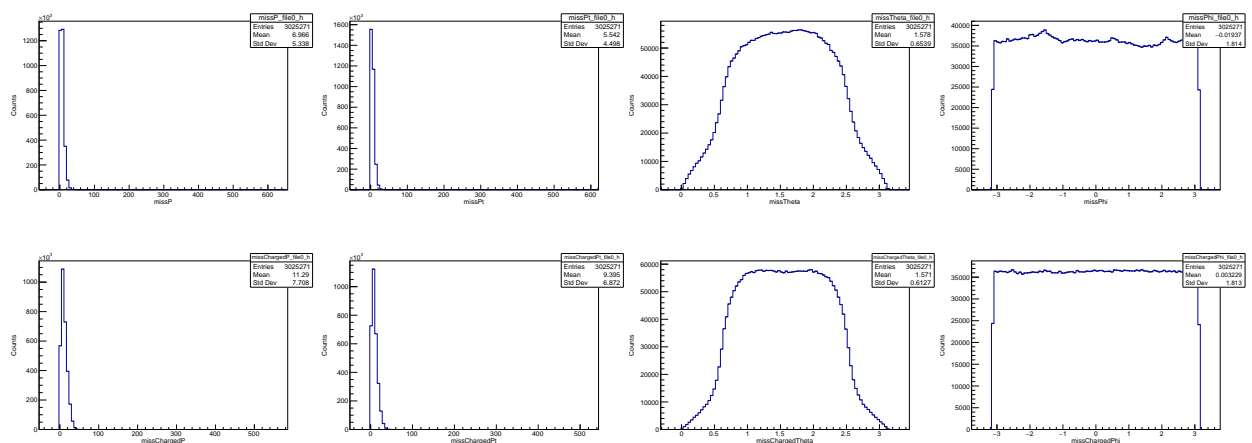


FIG. 12: LEP1 missing quantities distribution. Left to right: missing P ; missing p_t ; missing θ ; missing ϕ . Top to bottom: All; charged.

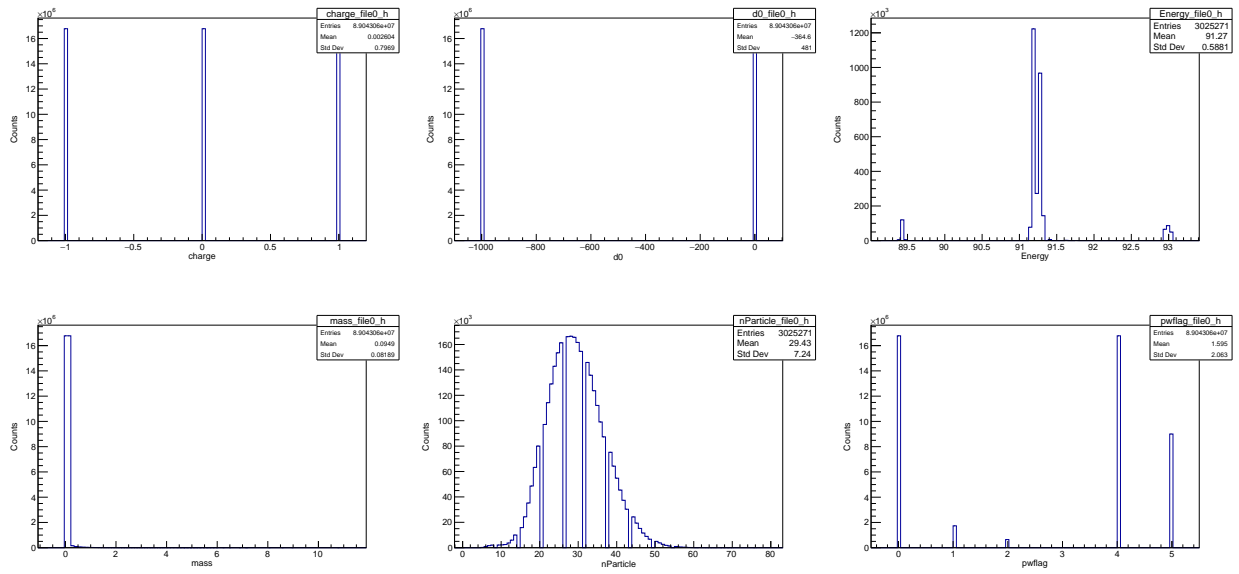


FIG. 13: Left to right: Top row: LEP1 charge, d_0 , and energy distributions. Bottom row: LEP1 mass, particle multiplicity, and pwflag distributions.

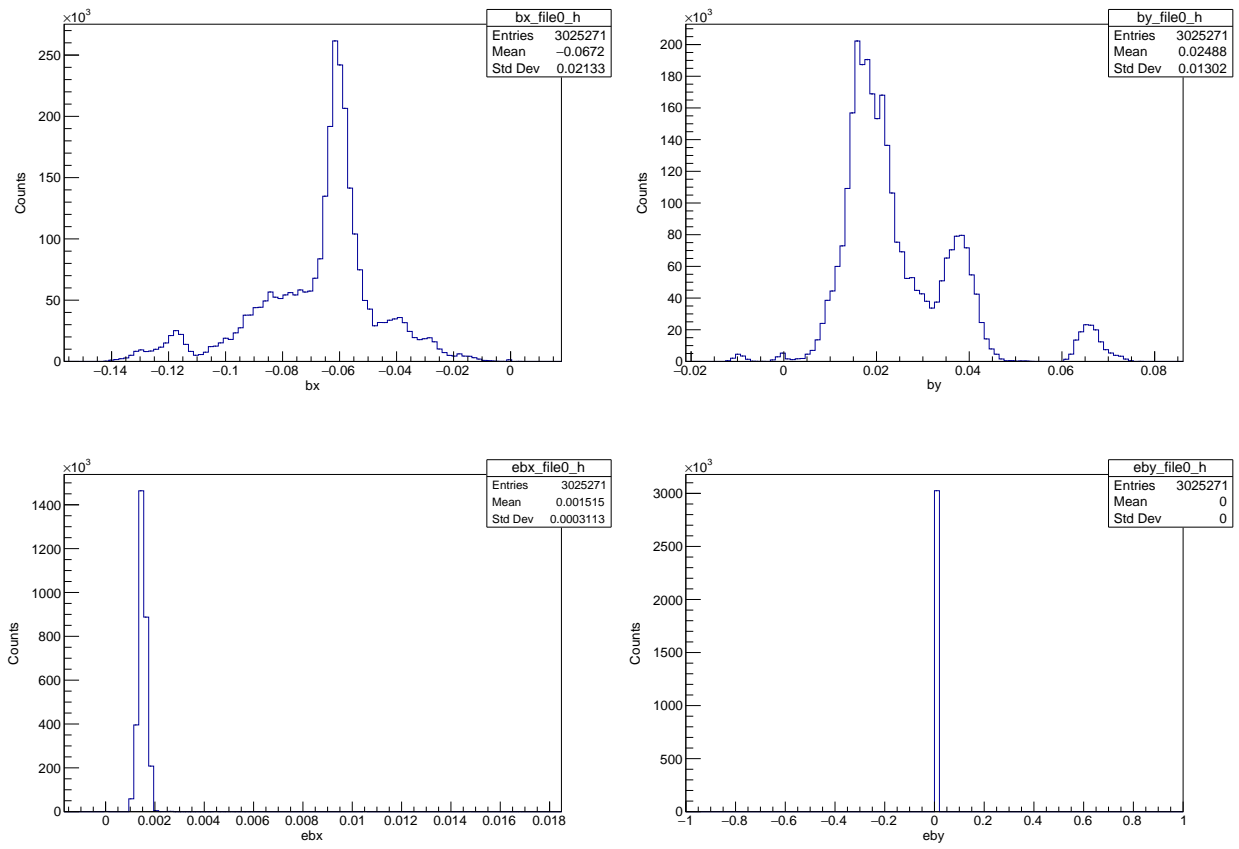


FIG. 14: Top row: LEP1 beamspot x and y . Bottom row: Error in beamspot x and y .

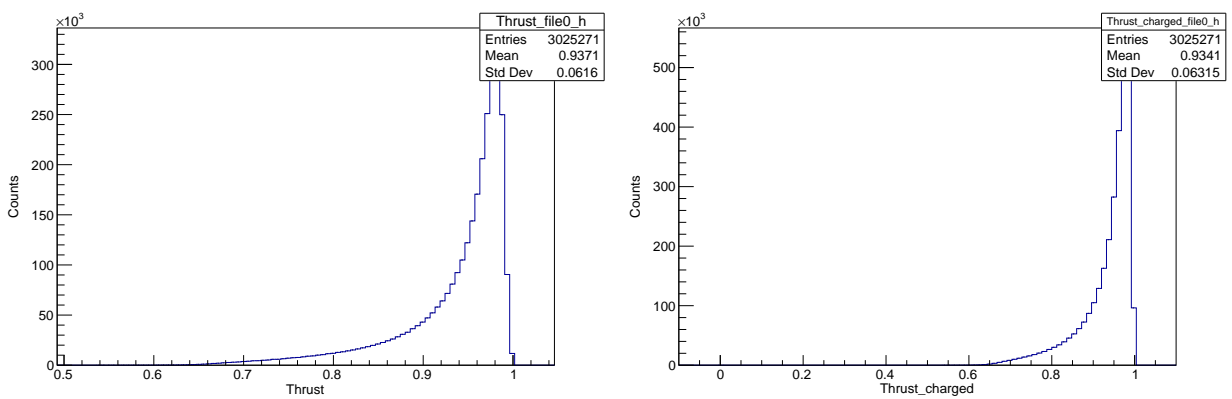


FIG. 15: Left: LEP1 thrust distribution. Right: LEP1 charged thrust distribution.

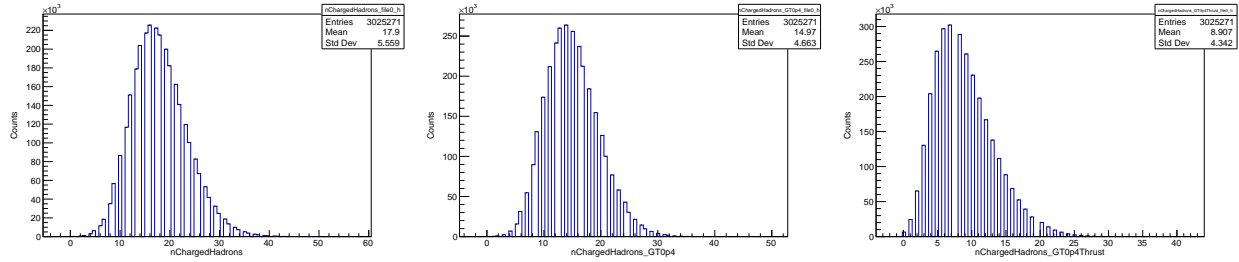


FIG. 16: LEP1 charged hadron multiplicity distributions. Left to right: charged hadron multiplicity; charged hadron multiplicity (GT0p4); charged hadron multiplicity (GT0p4Thrust).

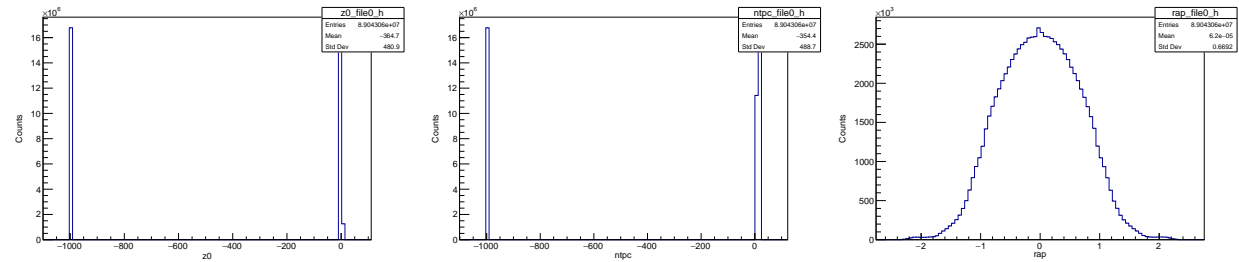


FIG. 17: Left: LEP1 z_0 distribution. Center: LEP1 TPC hits distribution. Right: LEP1 rapidity distribution.

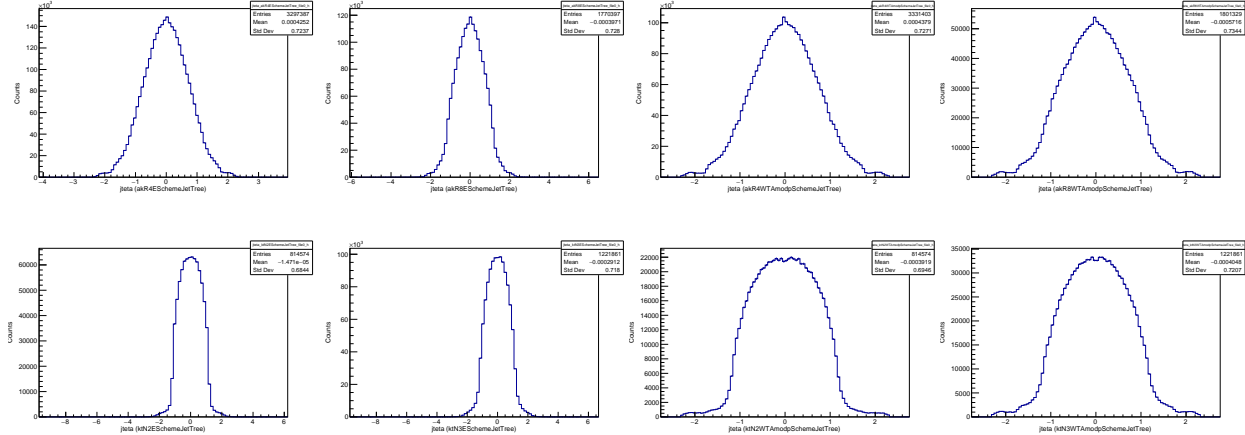


FIG. 18: LEP2 Jet η distributions. Top row: anti- k_t , left to right: $R = 0.4$, E scheme; $R = 0.8$, E scheme; $R = 0.4$, WTA mod p scheme; $R = 0.8$, WTA mod p scheme. Bottom row: k_t , left to right: $N = 2$, E scheme; $N = 3$, E scheme; $N = 2$, WTA mod p scheme; $N = 3$, WTA mod p scheme.

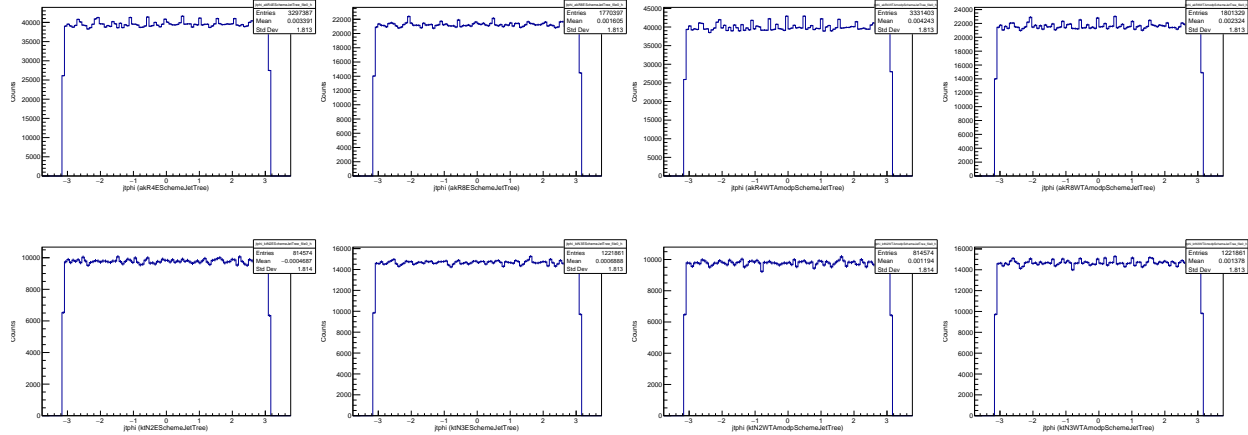


FIG. 19: LEP2 Jet ϕ distributions. Top row: anti- k_t , left to right: $R = 0.4$, E scheme; $R = 0.8$, E scheme; $R = 0.4$, WTA mod p scheme; $R = 0.8$, WTA mod p scheme. Bottom row: k_t , left to right: $N = 2$, E scheme; $N = 3$, E scheme; $N = 2$, WTA mod p scheme; $N = 3$; WTA mod p scheme.

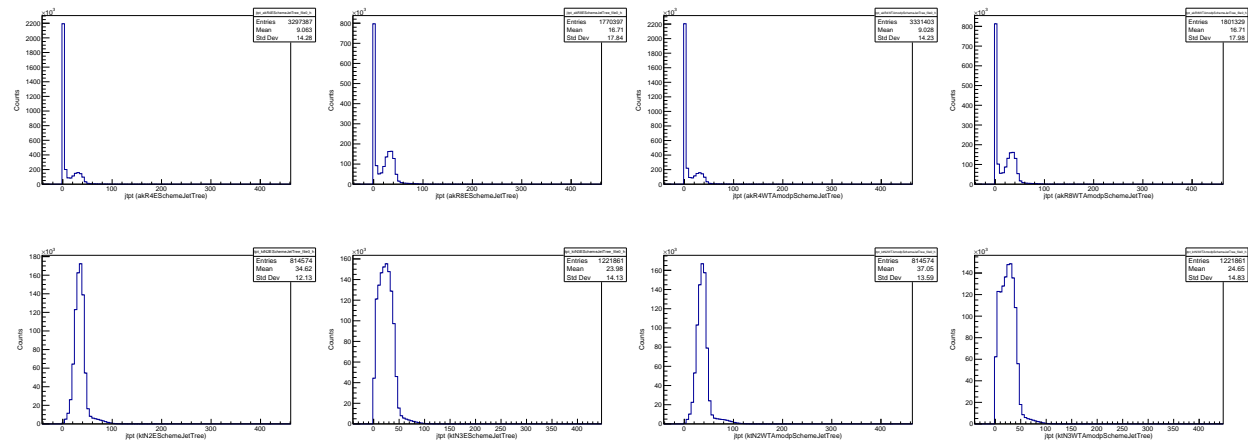


FIG. 20: LEP2 Jet p_t distributions. Top row: anti- k_t , left to right: $R = 0.4$, E scheme; $R = 0.8$, E scheme; $R = 0.4$, WTA mod p scheme; $R = 0.8$, WTA mod p scheme. Bottom row: k_t , left to right: $N = 2$, E scheme; $N = 3$, E scheme; $N = 2$, WTA mod p scheme; $N = 3$; WTA mod p scheme.

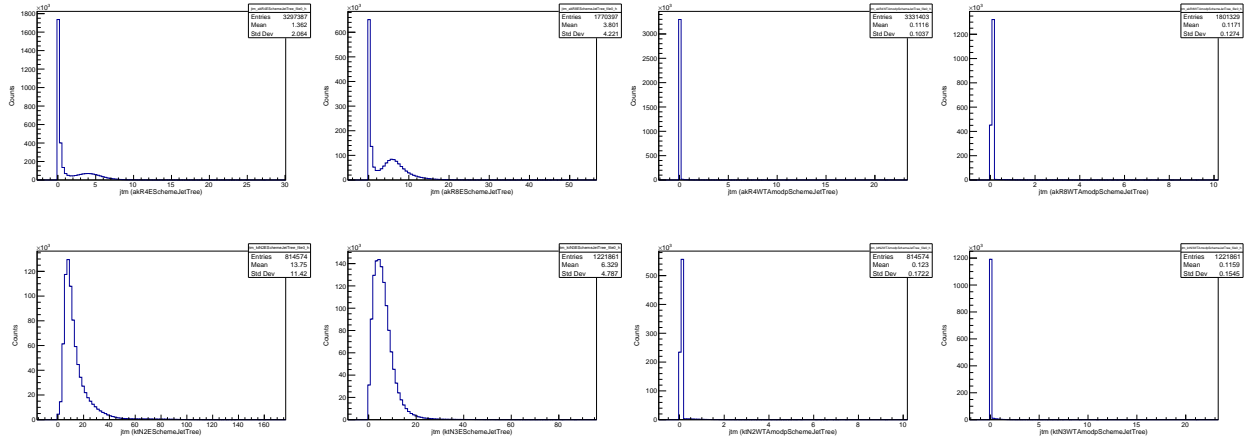


FIG. 21: LEP2 Jet mass distributions. Top row: anti- k_t , left to right: $R = 0.4$, E scheme; $R = 0.8$, E scheme; $R = 0.4$, WTA mod p scheme; $R = 0.8$, WTA mod p scheme. Bottom row: k_t , left to right: $N = 2$, E scheme; $N = 3$, E scheme; $N = 2$, WTA mod p scheme; $N = 3$; WTA mod p scheme.

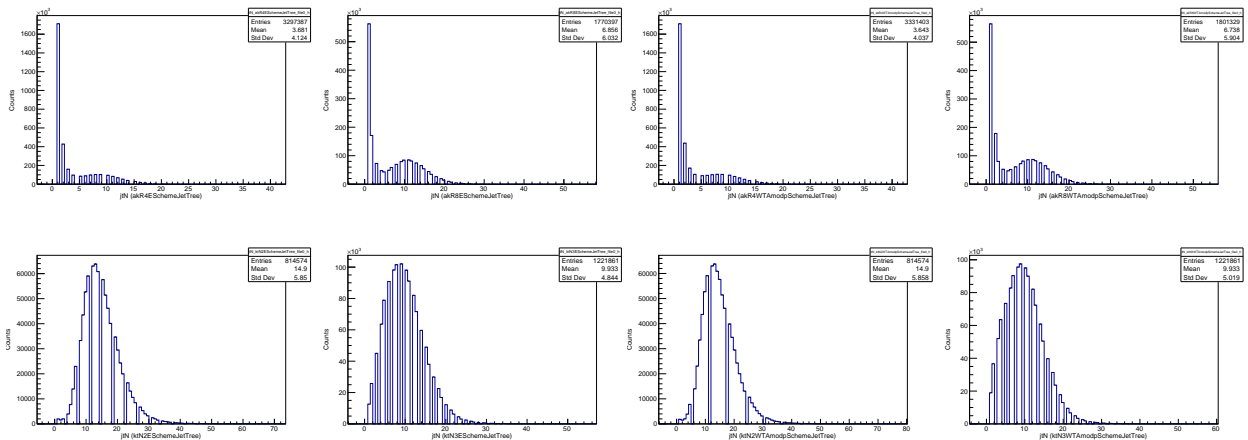


FIG. 22: LEP2 Jet N distributions. Top row: anti- k_t , left to right: $R = 0.4$, E scheme; $R = 0.8$, E scheme; $R = 0.4$, WTA mod p scheme; $R = 0.8$, WTA mod p scheme. Bottom row: k_t , left to right: $N = 2$, E scheme; $N = 3$, E scheme; $N = 2$, WTA mod p scheme; $N = 3$; WTA mod p scheme.

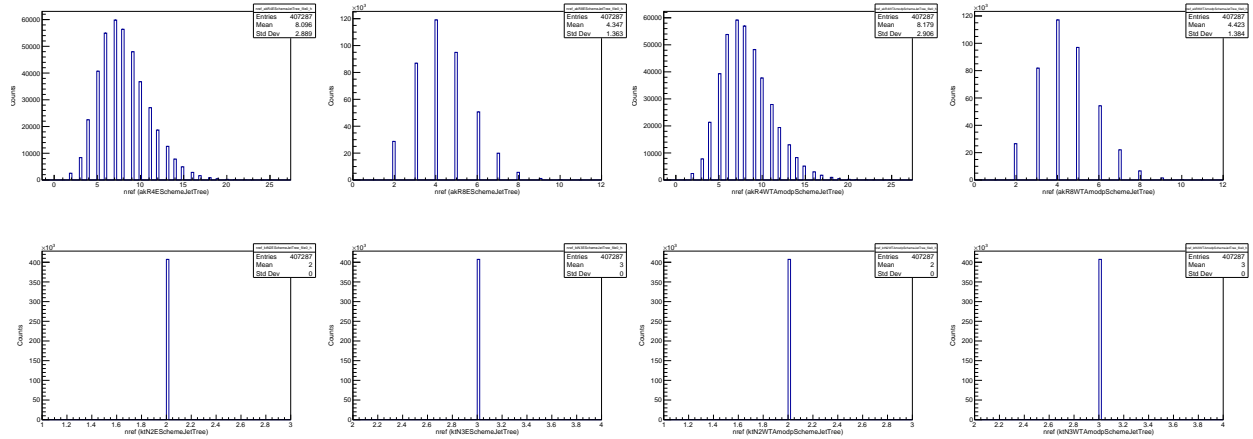


FIG. 23: LEP2 Jet n_{ref} distributions. Top row: anti- k_t , left to right: $R = 0.4$, E scheme; $R = 0.8$, E scheme; $R = 0.4$, WTA mod p scheme; $R = 0.8$, WTA mod p scheme. Bottom row: k_t , left to right: $N = 2$, E scheme; $N = 3$, E scheme; $N = 2$, WTA mod p scheme; $N = 3$; WTA mod p scheme.

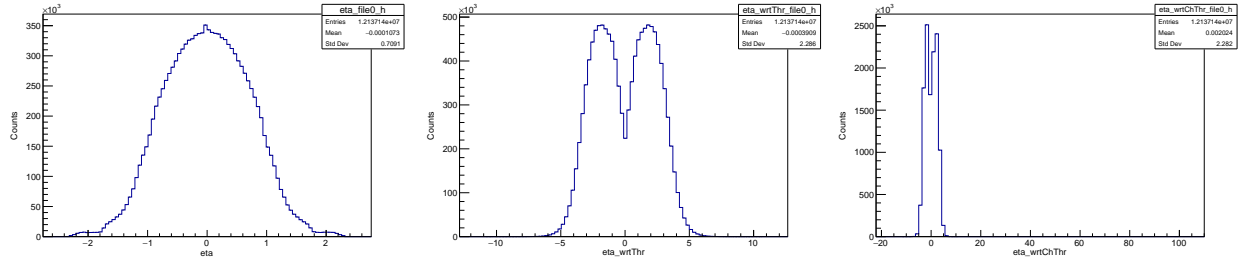


FIG. 24: LEP2 η distributions. Left to right: η ; η with respect to thrust axis; η with respect to charged thrust axis.

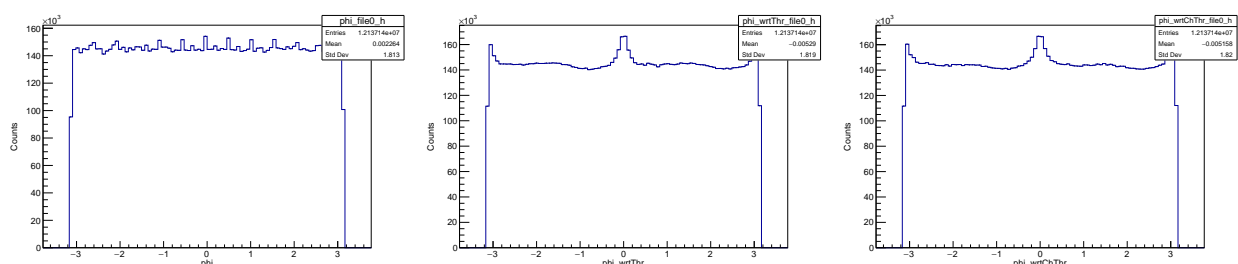


FIG. 25: LEP2 ϕ distributions. Left to right: ϕ ; ϕ with respect to thrust axis; ϕ with respect to charged thrust axis.

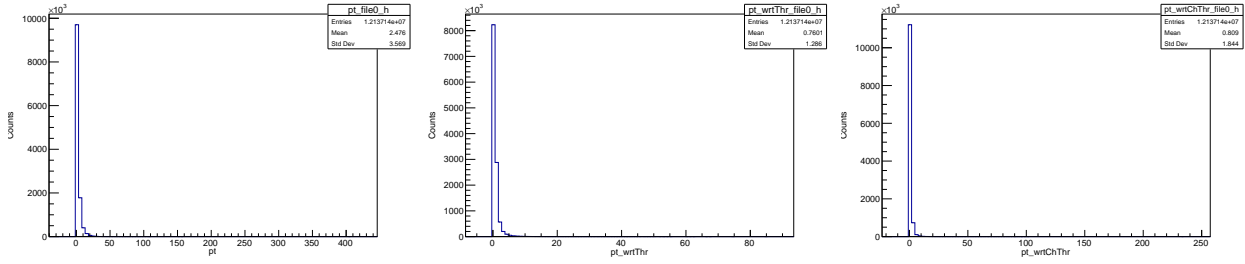


FIG. 26: LEP2 p_t distributions. Left to right: p_t ; p_t with respect to thrust axis; p_t with respect to charged thrust axis.

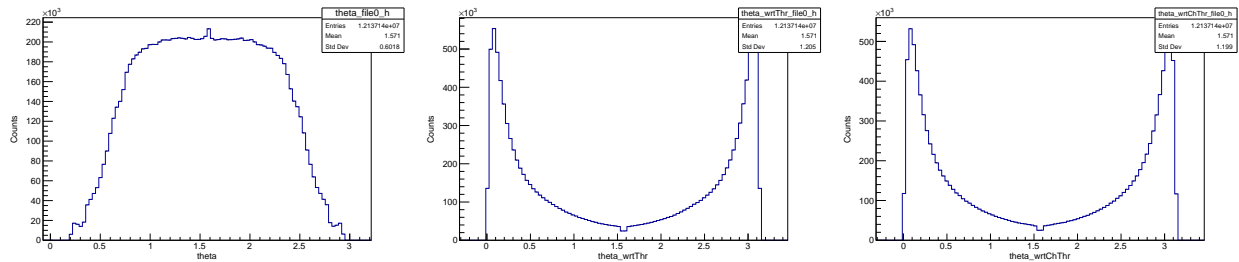


FIG. 27: LEP2 θ distributions. Left to right: θ ; θ with respect to thrust axis; θ with respect to charged thrust axis.

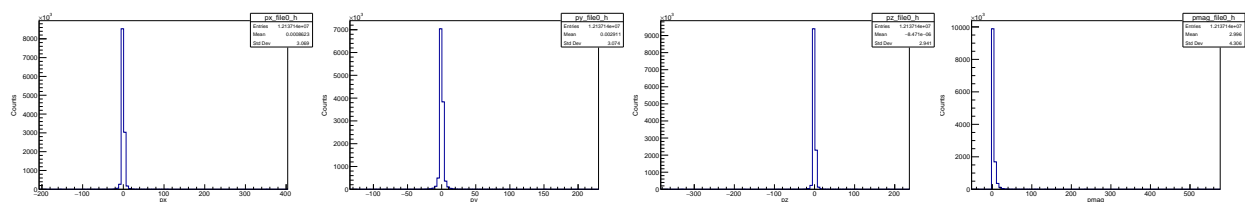


FIG. 28: LEP2 p_x , p_y , p_z , and $|\vec{p}|$ distributions.

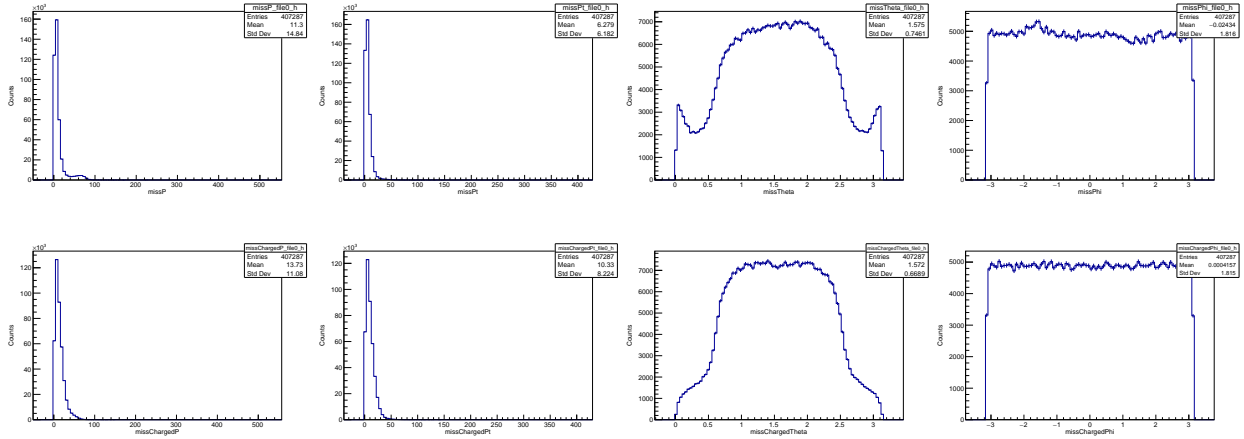


FIG. 29: LEP2 missing quantities distribution. Left to right: missing P ; missing p_t ; missing θ ; missing ϕ . Top to bottom: All; charged.

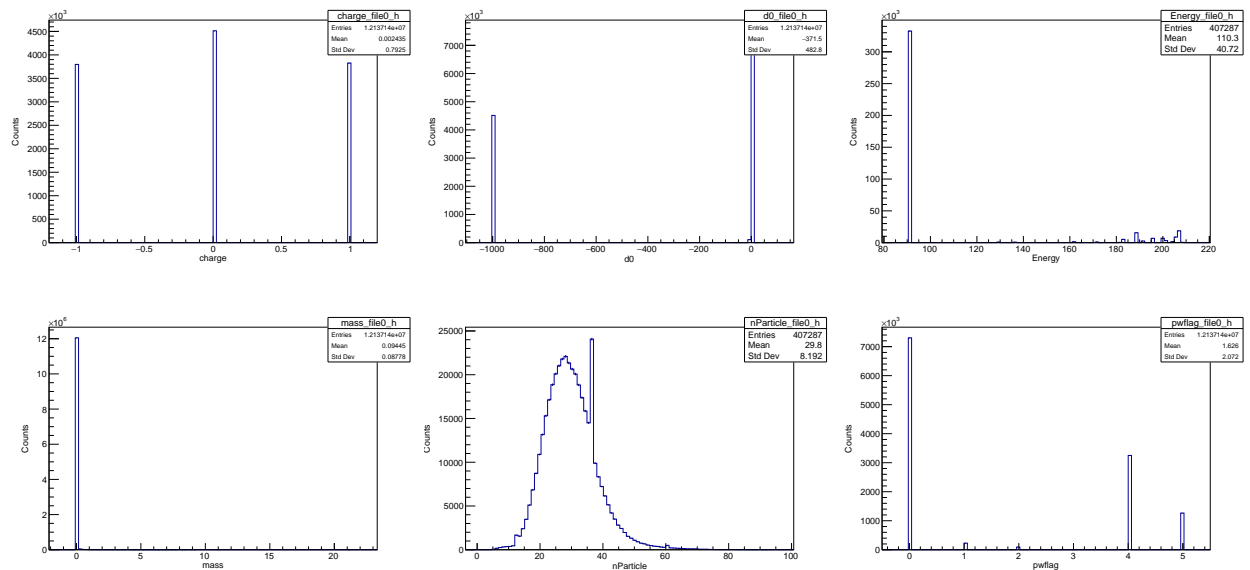


FIG. 30: Left to right: Top row: LEP2 charge, d_0 , and energy distributions. Bottom row: LEP2 mass, particle multiplicity, and pwflag distributions.

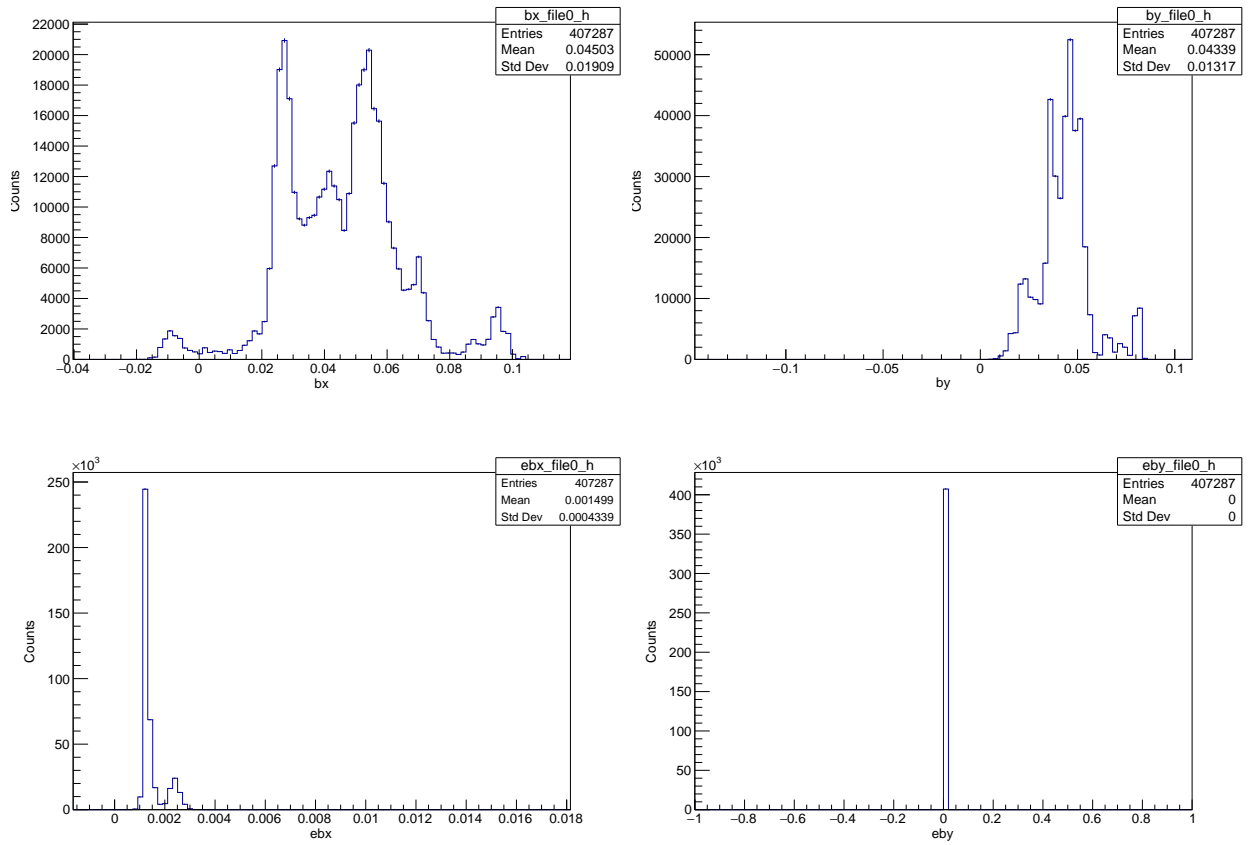


FIG. 31: Top row: LEP2 beamspot x and y . Bottom row: Error in beamspot x and y .

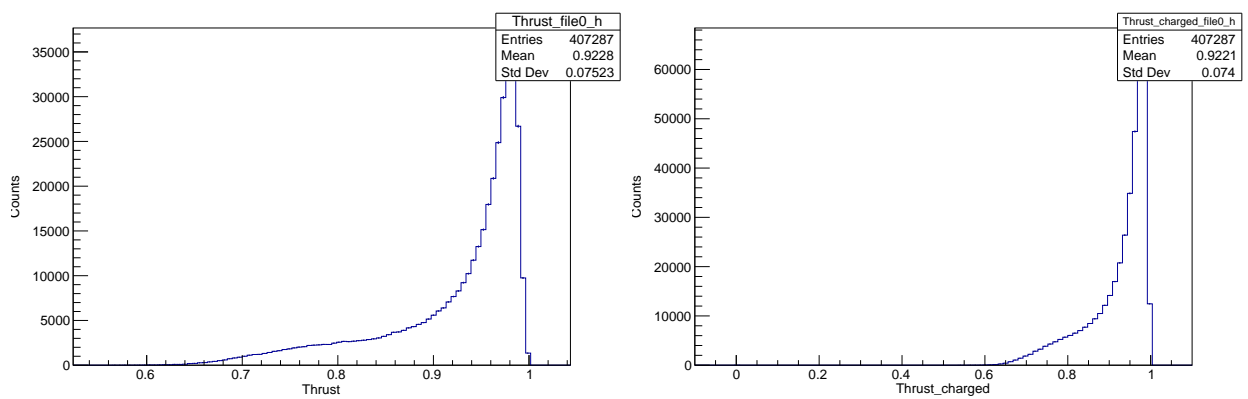


FIG. 32: Left: LEP2 thrust distribution. Right: LEP2 charged thrust distribution.

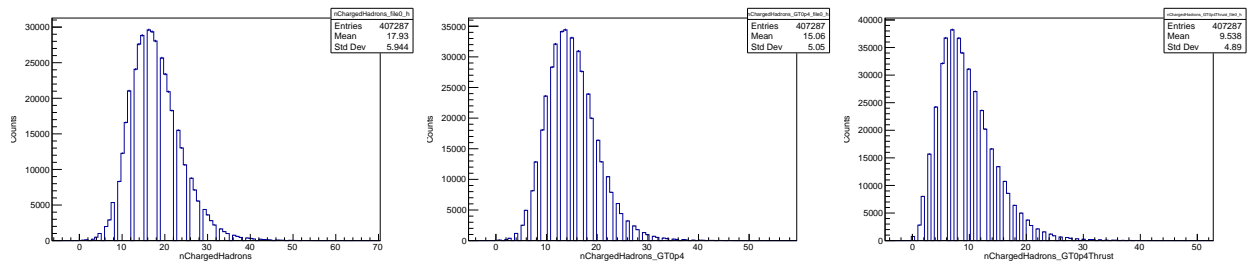
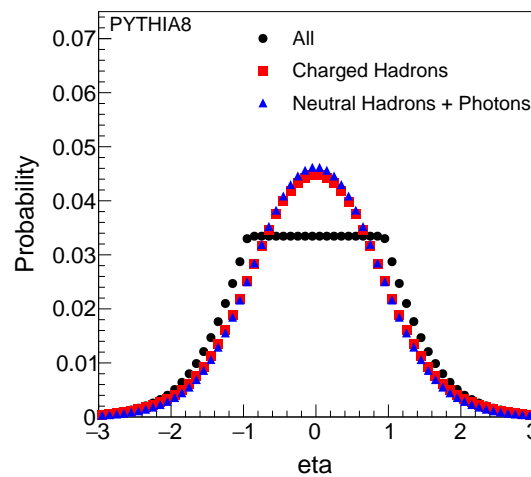
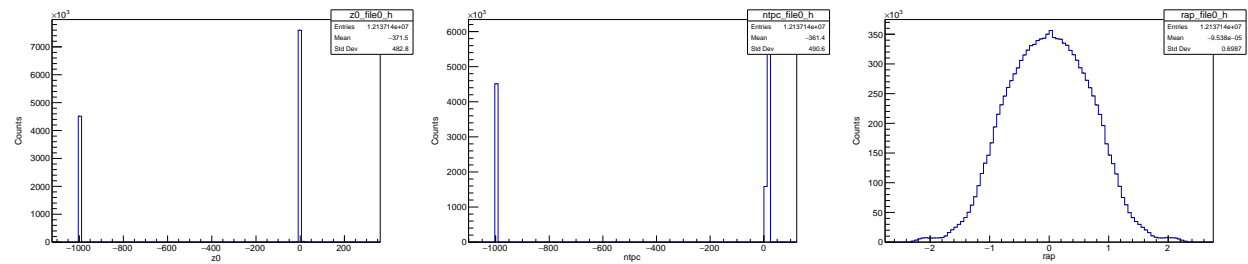


FIG. 33: LEP2 charged hadron multiplicity distributions. Left to right: charged hadron multiplicity; charged hadron multiplicity (GT0p4); charged hadron multiplicity (GT0p4Thrust).



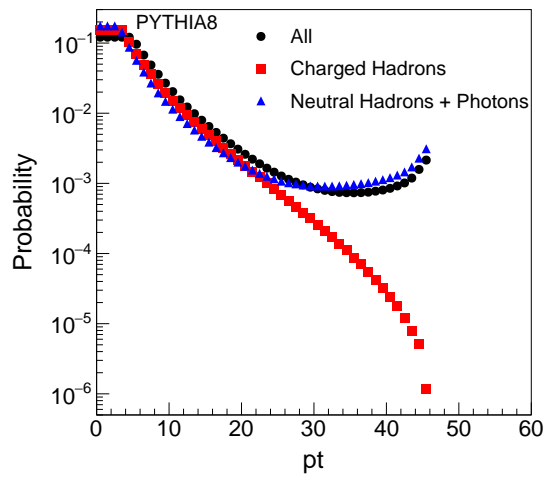


FIG. 36: PYTHIA8 PT spectra

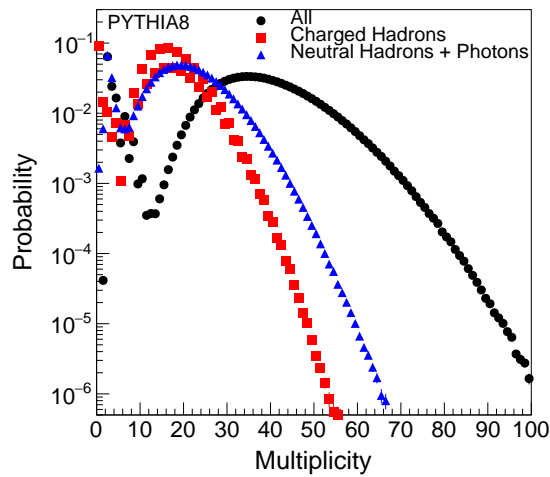


FIG. 37: PYTHIA8 Multiplicity Distribution

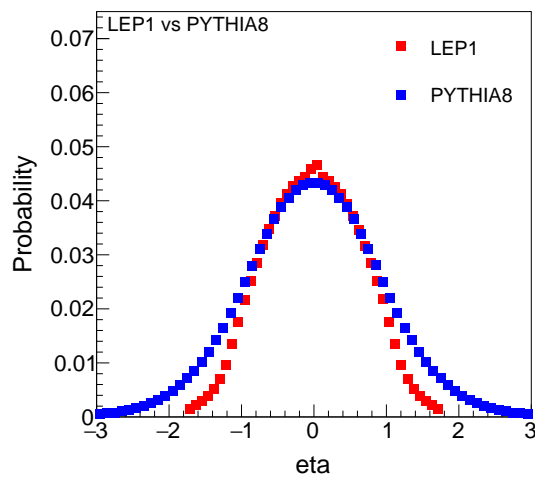


FIG. 38: LEP1 vs PYTHIA8 Eta Spectra of charged hadrons

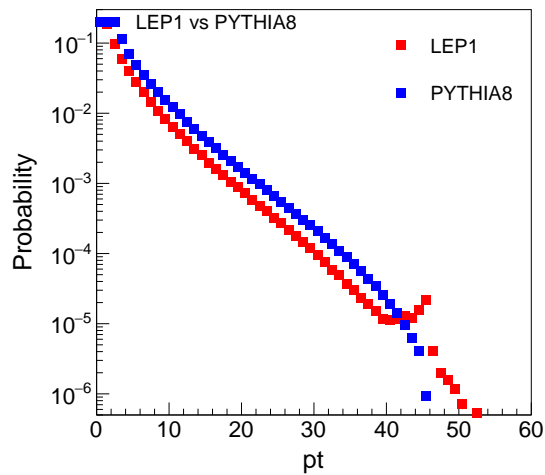


FIG. 39: LEP1 vs PYTHIA8 PT spectra of charged hadrons

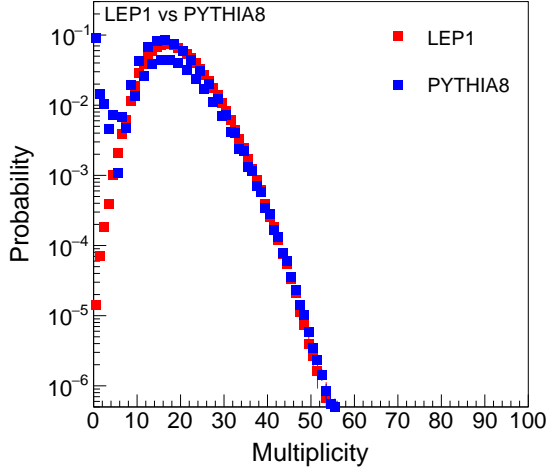


FIG. 40: LEP1 vs PYTHIA8 Multiplicity Distribution of charged hadrons

IV. MULTIPLICITY DISTRIBUTIONS

Previous measurements of two particle correlations have been done at hadron collider experiments, such as CMS. These measurements typically are typically done in bins of event multiplicity in order to quantify the activity in a set of events. Because ALEPH has a different acceptance than the CMS detector, and because e^+e^- collisions have different kinematics than those at hadron colliders, some conversion needs to be done in order to compare events of a given multiplicity in ALEPH with those in CMS. For the studies done here, we require charged tracks to have $p_T < 0.2$ GeV and $|\eta| < 1.8$ in ALEPH, and $p_T < 0.4$ and $|\eta| < 2.4$ in CMS. The latter requirement is identical to the cuts used in all CMS papers on two particle correlations. The multiplicity distribution in LEP1 ALEPH events can be seen in Fig. ???. The tracking efficiency as a function of event multiplicity can be seen in Fig. ???, calculated by matching reconstructed tracks to generator-level particles in ALEPH Monte Carlo. The dip at low multiplicity is most likely due to a self-bias causing low-efficiency events to also have low multiplicity. After taking into account both the efficiency and acceptance of the ALEPH detector, the total fraction of charged particles reconstructed is shown in Fig. ???. In the highest multiplicity events, the ALEPH detector reconstructions around 50% of all the charged particles in an event.

The acceptance of the CMS detector, as calculated by seeing how many generator-level

charged particles pass the η cut, in pp pythia Monte Carlo events is shown in Fig. ???. This is done as a function of generator-level multiplicity. Roughly 30% of all charged particles can be reconstructed in CMS for pp collisions. Using Fig. ?? and Fig. ??, a conversion factor can be calculated to convert the reconstructed ALEPH multiplicity to an equivalent corrected multiplicity for a hadron collider. This conversion factor is shown in Fig. ??, and the mapping from ALEPH multiplicities to CMS multiplicities is shown in Fig. ???. The behavior at low multiplicities is caused by the self-bias of the efficiency and acceptances with the multiplicity calculation. However, this analysis is mostly interested in events having high multiplicity, where the conversion factor converges to a reasonable factor of around 0.7. After applying this mapping to the distribution in Fig. ??, the multiplicity distribution that can be used for comparing with CMS results is shown in Fig. ??.

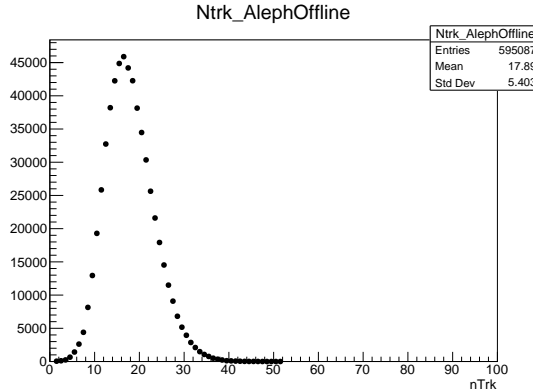


FIG. 41: LEP1 Multiplicity Distribution

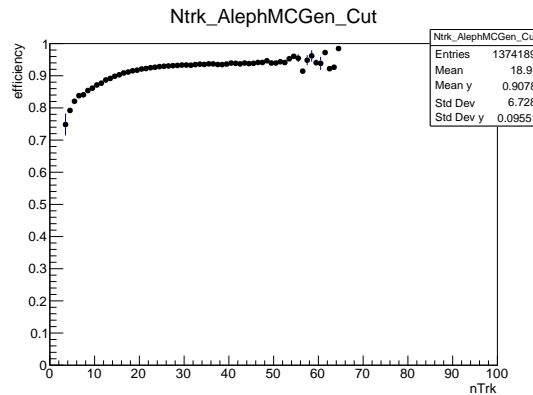


FIG. 42: LEP1 Efficiency Distribution vs Multiplicity

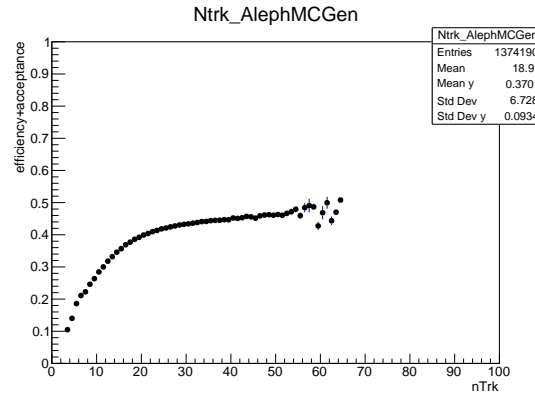


FIG. 43: LEP1 Efficiency+Acceptance Distribution vs Multiplicity

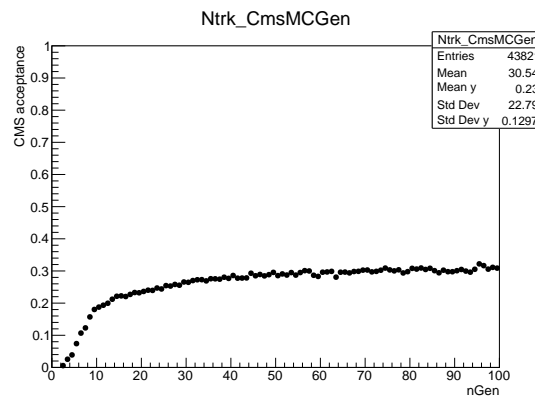


FIG. 44: CMS Acceptance Distribution vs generator-level Multiplicity

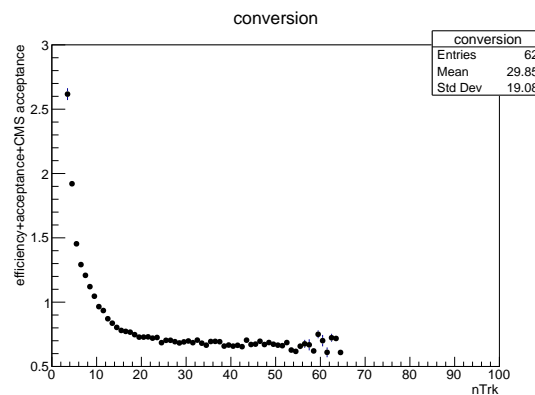


FIG. 45: Conversion factor from ALEPH to CMS multiplicity

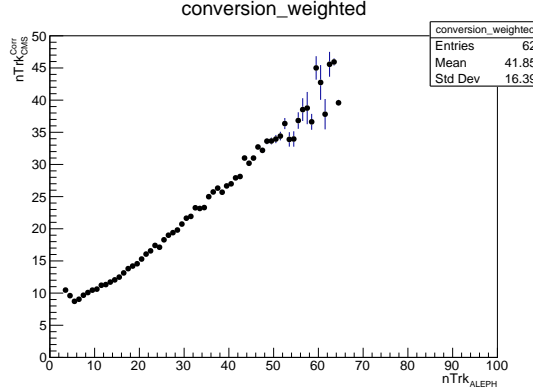


FIG. 46: Conversion mapping from ALEPH to CMS multiplicity

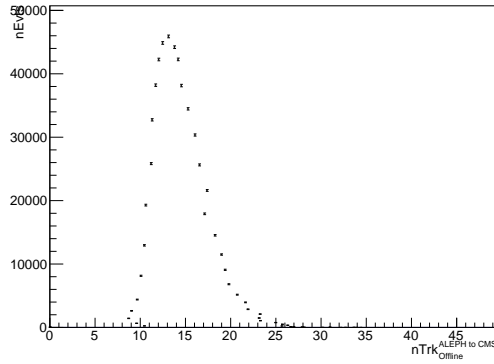


FIG. 47: Scaled ALEPH multiplicity for comparing to CMS

V. ANALYSIS

VI. THRUST AXIS

VII. REPRODUCING QCD PAPER PLOT

VIII. TWO-PARTICLE CORRELATION FUNCTION

In this analysis with ALEPH open data, charged particles with transverse momentum between 0.1 and 4.0 GeV/ c are selected for the correlation function analysis. High multiplicity events are sampled using the total number of selected proton, pions and kaons (hadron multiplicity N) in each event. The first step in extracting the correlation function was to divide the sample into bins in the hadron multiplicity. For each hadron multiplicity class, “trig-

ger” particles are defined as charged hadrons in the selected transverse momentum range (0.1 and 4.0 GeV/ c). Particle pairs are then formed by associating every trigger particle with the remaining charged hadrons in the same p_T interval as the trigger particle. The per-trigger-particle associated yield is defined as:

$$\frac{1}{N_{\text{trig}}} \frac{d^2N^{\text{pair}}}{d\Delta\eta d\Delta\phi} = B(0, 0) \times \frac{S(\Delta\eta, \Delta\phi)}{B(\Delta\eta, \Delta\phi)} \quad (1)$$

where N_{trig} is the number of trigger particles in the event, $\Delta\eta$ and $\Delta\phi$ are the differences in η and ϕ of the pair. The signal distribution, $S(\Delta\eta, \Delta\phi)$, is the per-trigger-particle yield of particle pairs in the same event:

$$S(\Delta\eta, \Delta\phi) = \frac{1}{N_{\text{trig}}} \frac{d^2N^{\text{same}}}{d\Delta\eta d\Delta\phi} \quad (2)$$

The mixed-event background distribution, used to account for random combinatorial background, is defined as

$$B(\Delta\eta, \Delta\phi) = \frac{1}{N_{\text{trig}}} \frac{d^2N^{\text{mix}}}{d\Delta\eta d\Delta\phi} \quad (3)$$

and is constructed by pairing the trigger particles from two random events in the same hadron multiplicity interval. The symbol N^{mix} denotes the number of pairs taken from the mixed event, while $B(0, 0)$ represents the mixed-event associated yield for both particles of the pair going in the same direction and thus having full pair acceptance. Therefore, the ratio $B(0, 0)/B(\Delta\eta, \Delta\phi)$ represents the pair-acceptance correction factor used to derive the corrected per-trigger-particle associated yield distribution. The signal and background distributions are first calculated for each event and then averaged over all the events within the track multiplicity class.

In the full data analysis, a matching between particles and the primary vertex should be performed so that the studies are done with primary hadrons from a single primary vertex. This matching requirement is not yet included in this preliminary analysis due to the limited information in the Belle open data.

Two particle correlation functions for the LEP1 and LEP2 data sets analyzed in the beam, thrust, and winner-take-all (WTA) axes are shown below. The first row contains events with $n_{\text{Trk}} < 20$, the second with $20 \leq n_{\text{Trk}} < 30$, and third with $30 \leq n_{\text{Trk}}$.

Date	Axis	p_T	$ \eta $	θ	p	$ dxy $	$ dz $	nTPC
2018.01.26	Beam	≥ 0.4	<1.8	off	off	off	off	off
	Thrust	≥ 0.4	<5.0	off	off	off	off	off
	WTA	≥ 0.4	<5.0	off	off	off	off	off
2018.02.XX	Beam	≥ 0.4	<1.8	[20,160]	>0.2	<3.0	<5.0	≥ 4.0
	Thrust	≥ 0.4	<5.0	[20,160]	>0.2	<3.0	<5.0	≥ 4.0
	WTA	≥ 0.4	<5.0	[20,160]	>0.2	<3.0	<5.0	≥ 4.0

TABLE I: Track cuts for Beam, Thrust, and WTA axes.

Date	Axis	WW	p_{miss}	2-Jet	p_{miss}^{rel}	3rd-Jet	$p_{1,2}^{rel}$	N_{trk}
2018.01.26	Beam	off	off	off	off	off	off	>1
	Thrust	off	off	off	off	off	off	>1
	WTA	off	off	off	off	off	off	>1
2018.02.XX	Beam	off	≤ 20	0.1	0.03	0.03	0.03	>1
	Thrust	off	≤ 20	0.1	0.03	0.03	0.03	>1
	WTA	off	≤ 20	0.1	0.03	0.03	0.03	>1

TABLE II: Event cuts for Beam, Thrust, and WTA axes.

A. Analysis for 2018.01.26 production

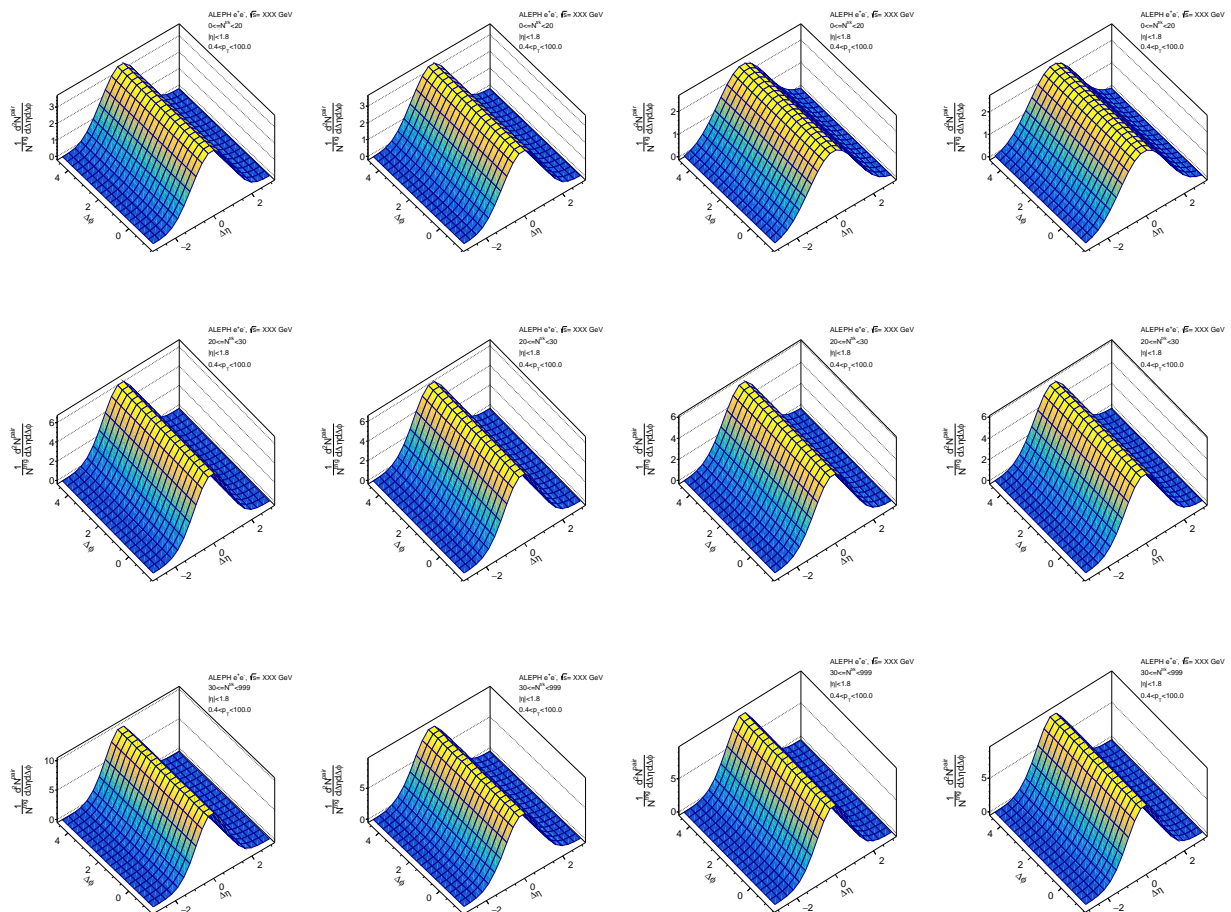


FIG. 48: Background function for beam axis. Left to right: LEP1, LEP2, PYTHIA8, PYTHIA8 rope walk. Top to bottom: multiplicity 0-20, 20-30, 30-999.

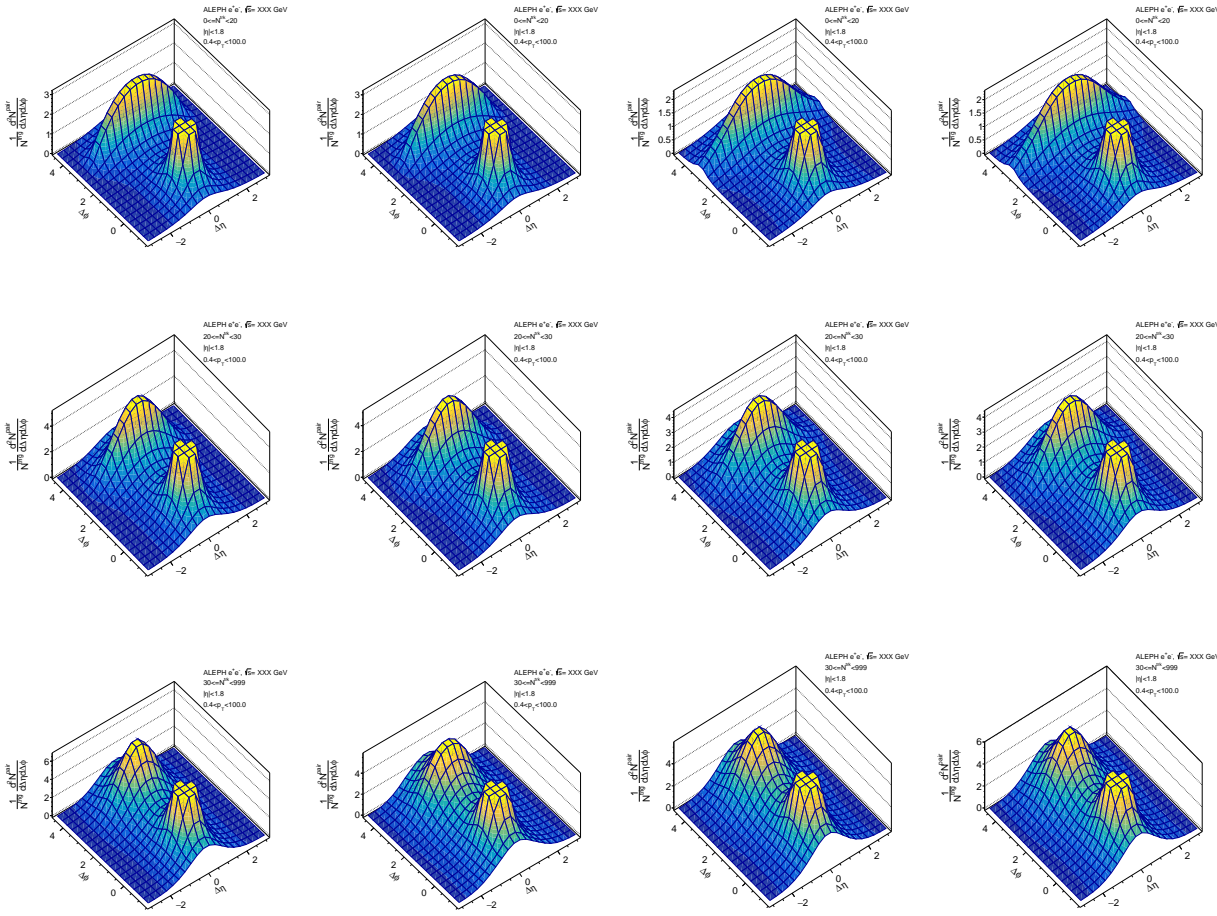


FIG. 49: Signal function for beam axis. Left to right: LEP1, LEP2, PYTHIA8, PYTHIA8 rope walk. Top to bottom: multiplicity 0-20, 20-30, 30-999.

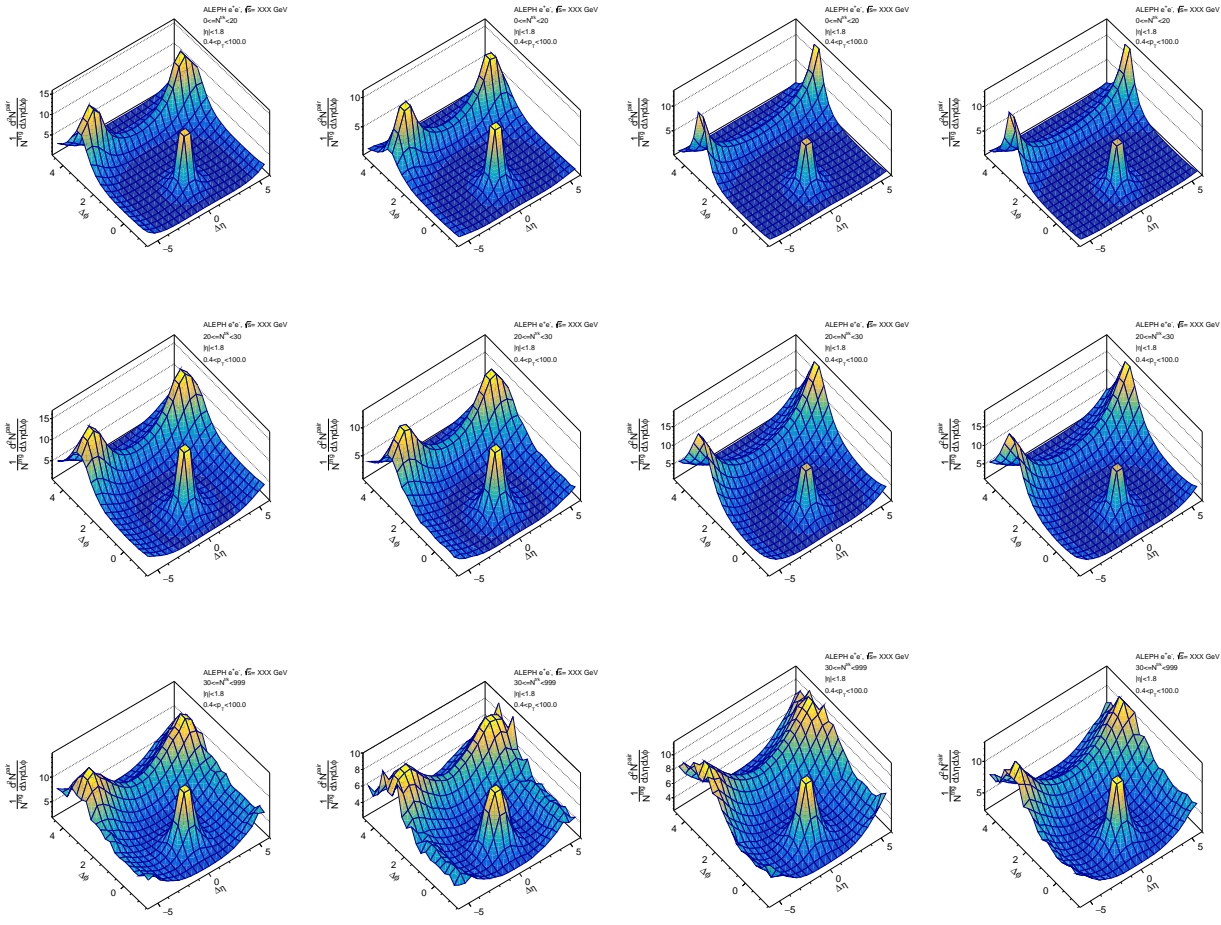
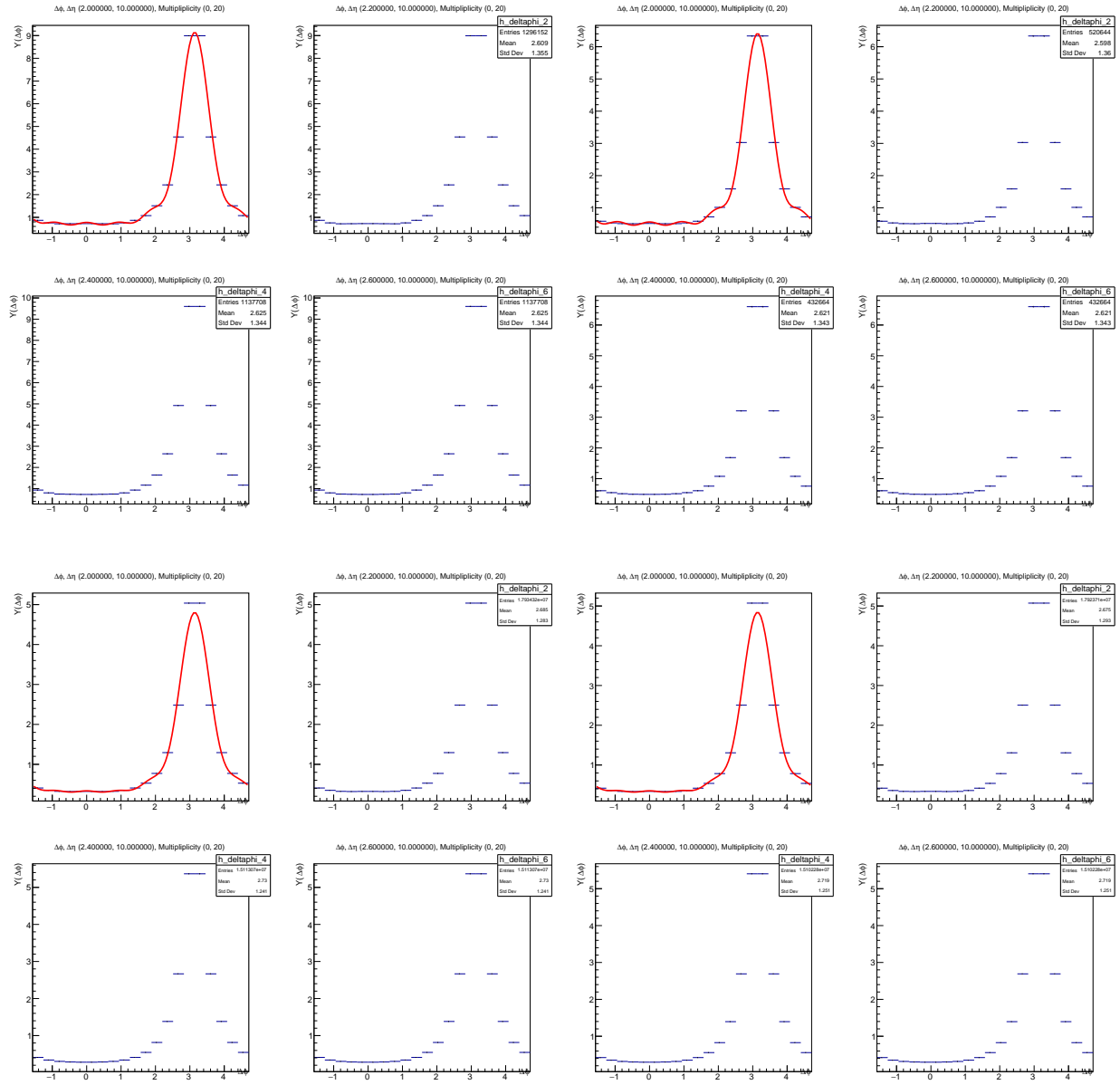


FIG. 50: Ratio function for beam axis. Left to right: LEP1, LEP2, PYTHIA8, PYTHIA8 rope walk. Top to bottom: multiplicity 0-20, 20-30, 30-999.



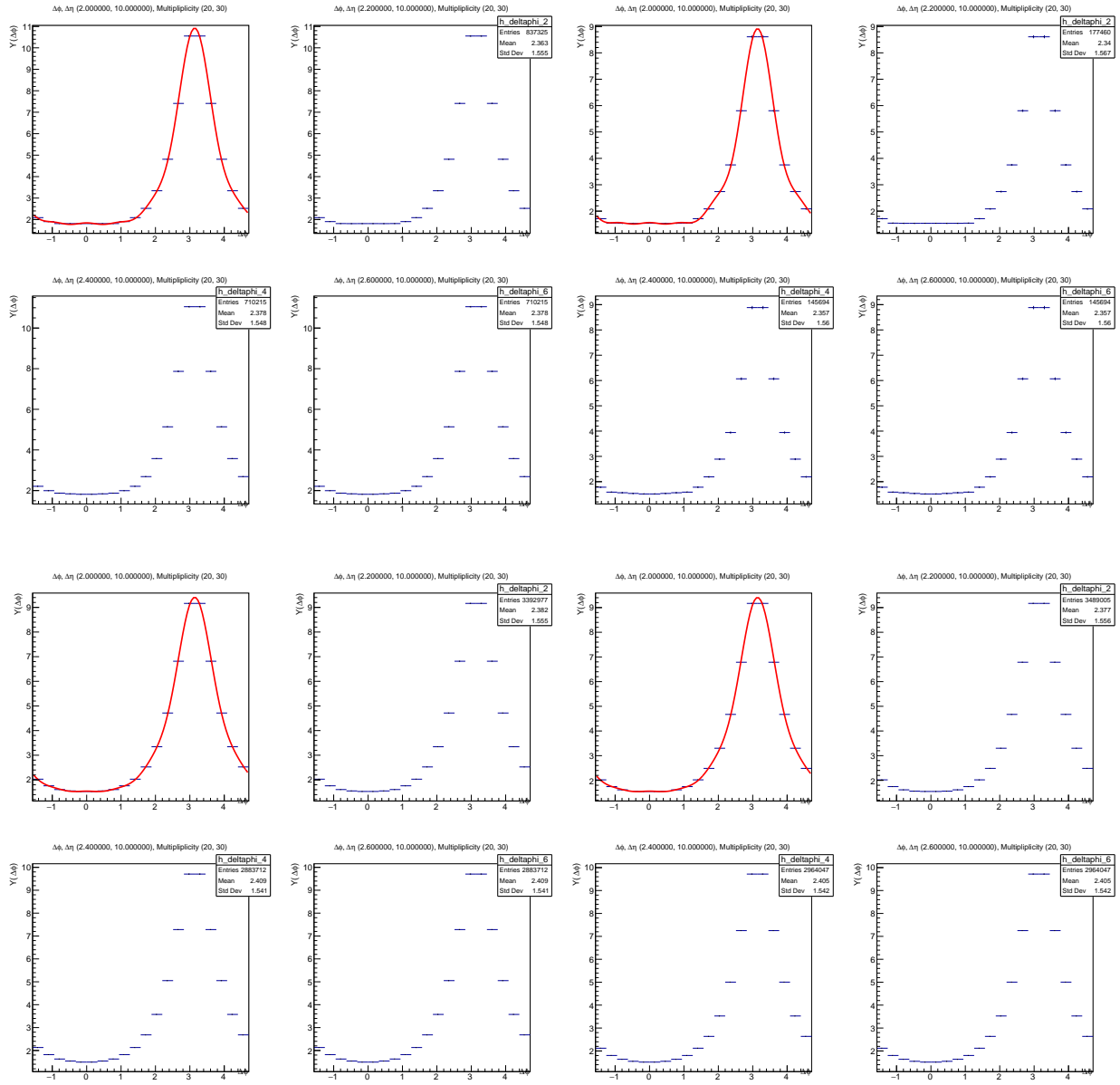


FIG. 52: Long range yield function for beam axis. Top row is LEP1 and LEP2, bottom row PYTHIA8 and PYTHIA8 rope walk. Multiplicity 20-30.

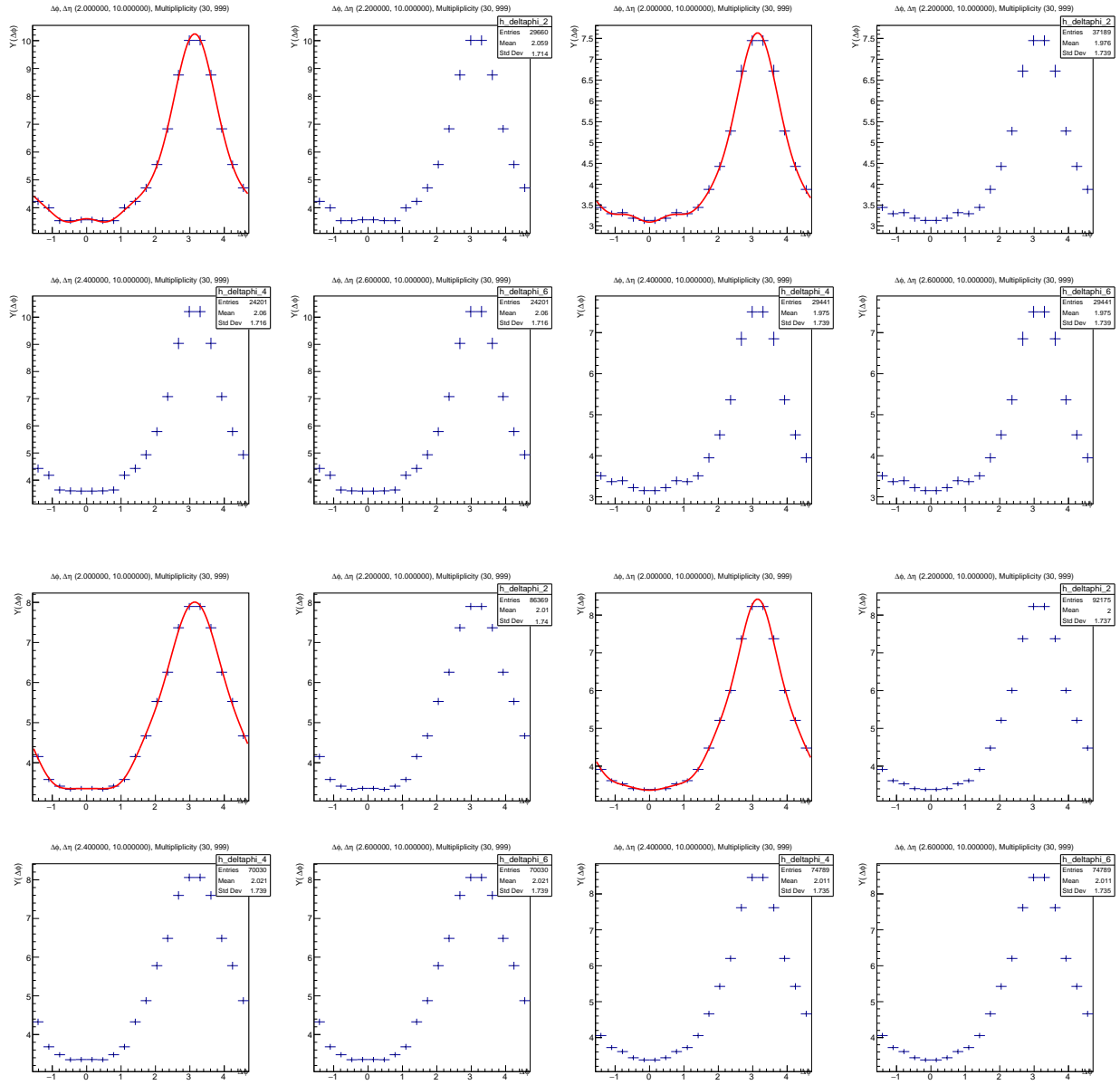


FIG. 53: Long range yield function for beam axis. Top row is LEP1 and LEP2, bottom row PYTHIA8 and PYTHIA8 rope walk. Multiplicity 30-999.

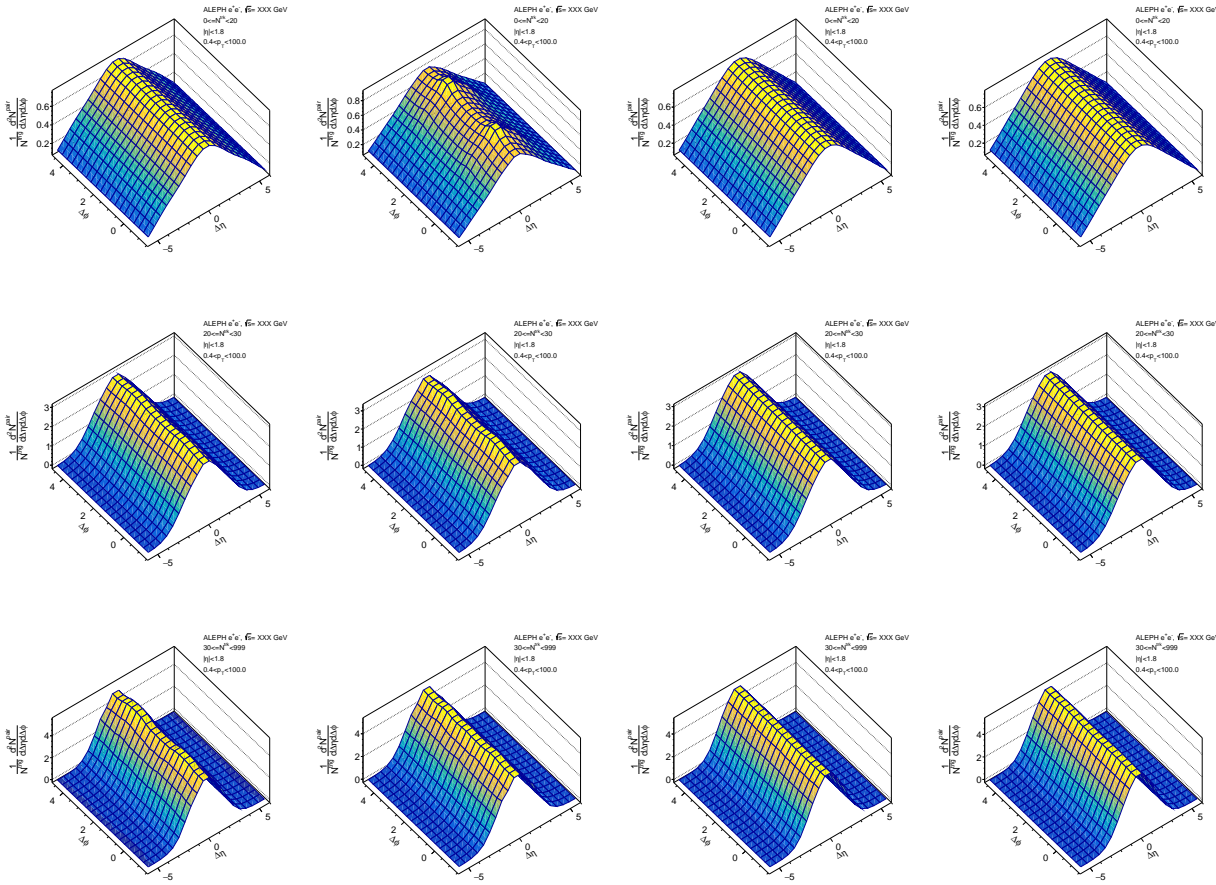


FIG. 54: Background function for thrust axis. Left to right: LEP1, LEP2, PYTHIA8, PYTHIA8 rope walk. Top to bottom: multiplicity 0-20, 20-30, 30-999.

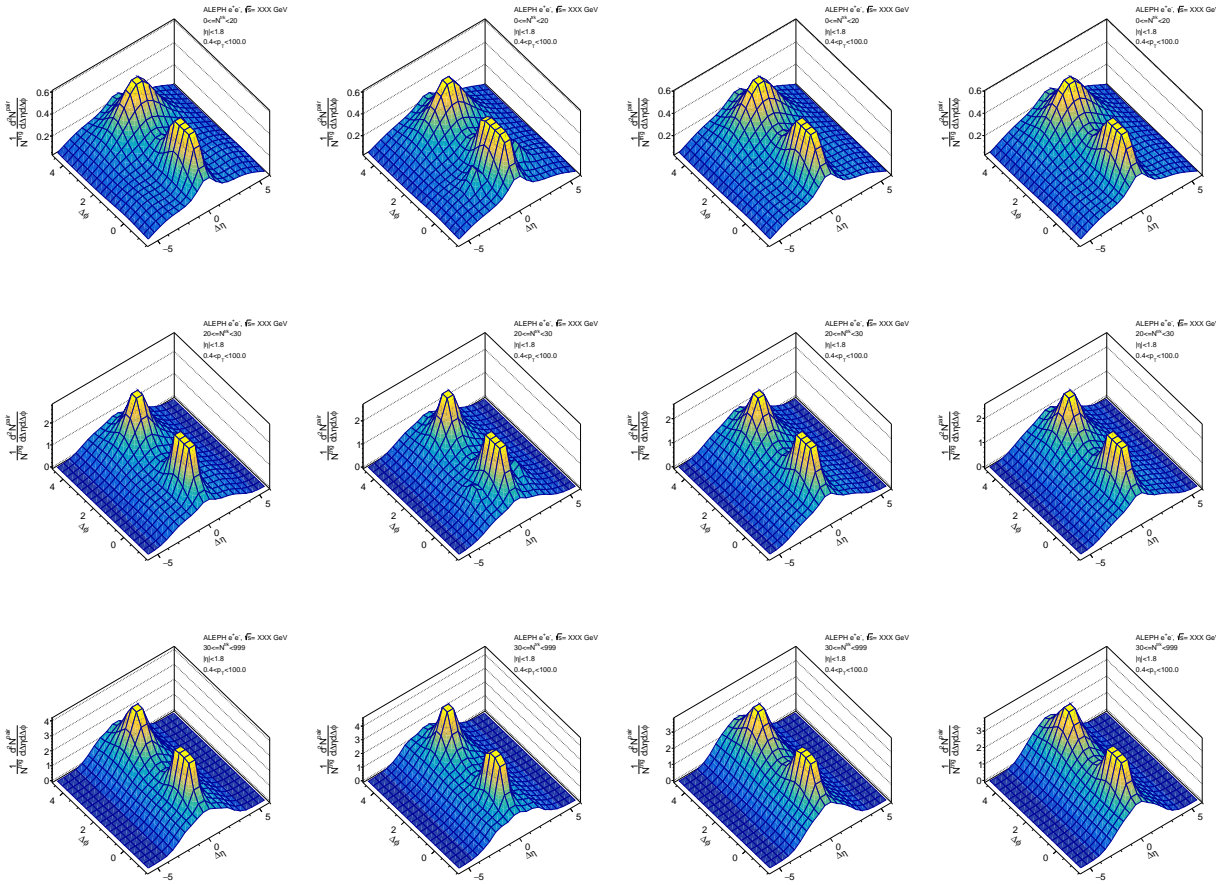


FIG. 55: Signal function for thrust axis. Left to right: LEP1, LEP2, PYTHIA8, PYTHIA8 rope walk. Top to bottom: multiplicity 0-20, 20-30, 30-999.

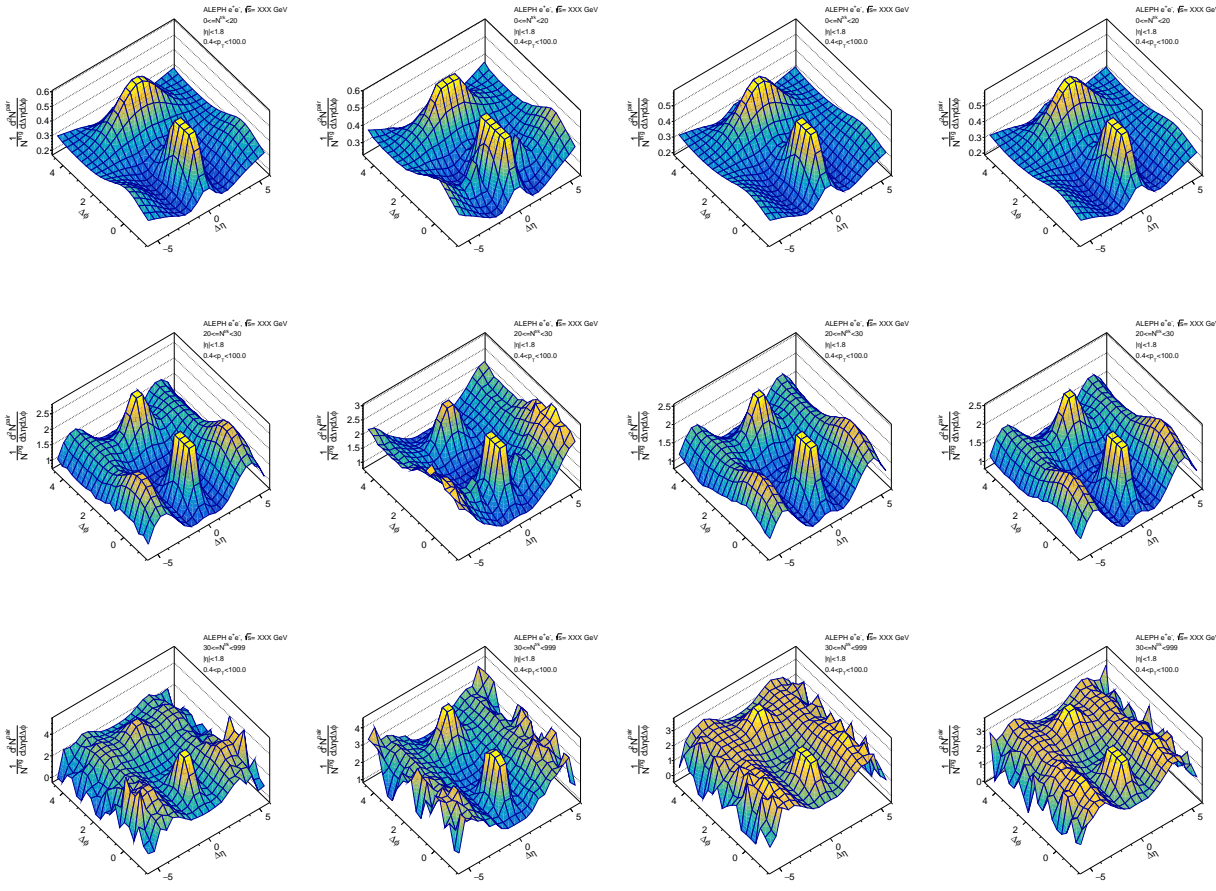


FIG. 56: Ratio function for thrust axis. Left to right: LEP1, LEP2, PYTHIA8, PYTHIA8 rope walk. Top to bottom: multiplicity 0-20, 20-30, 30-999.

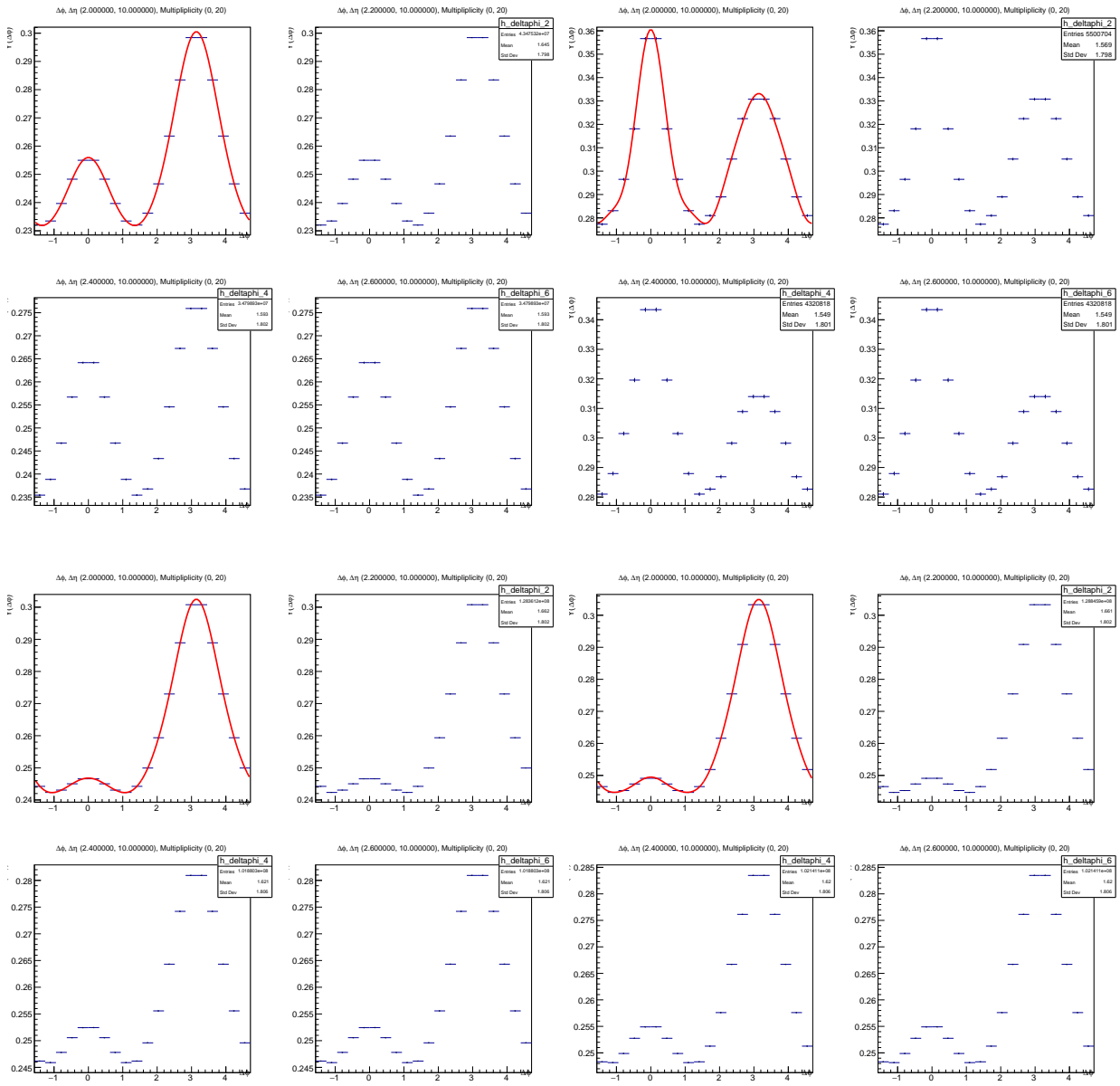


FIG. 57: Long range yield function for thrust axis. Top row is LEP1 and LEP2, bottom row PYTHIA8 and PYTHIA8 rope walk. Multiplicity 0-20.

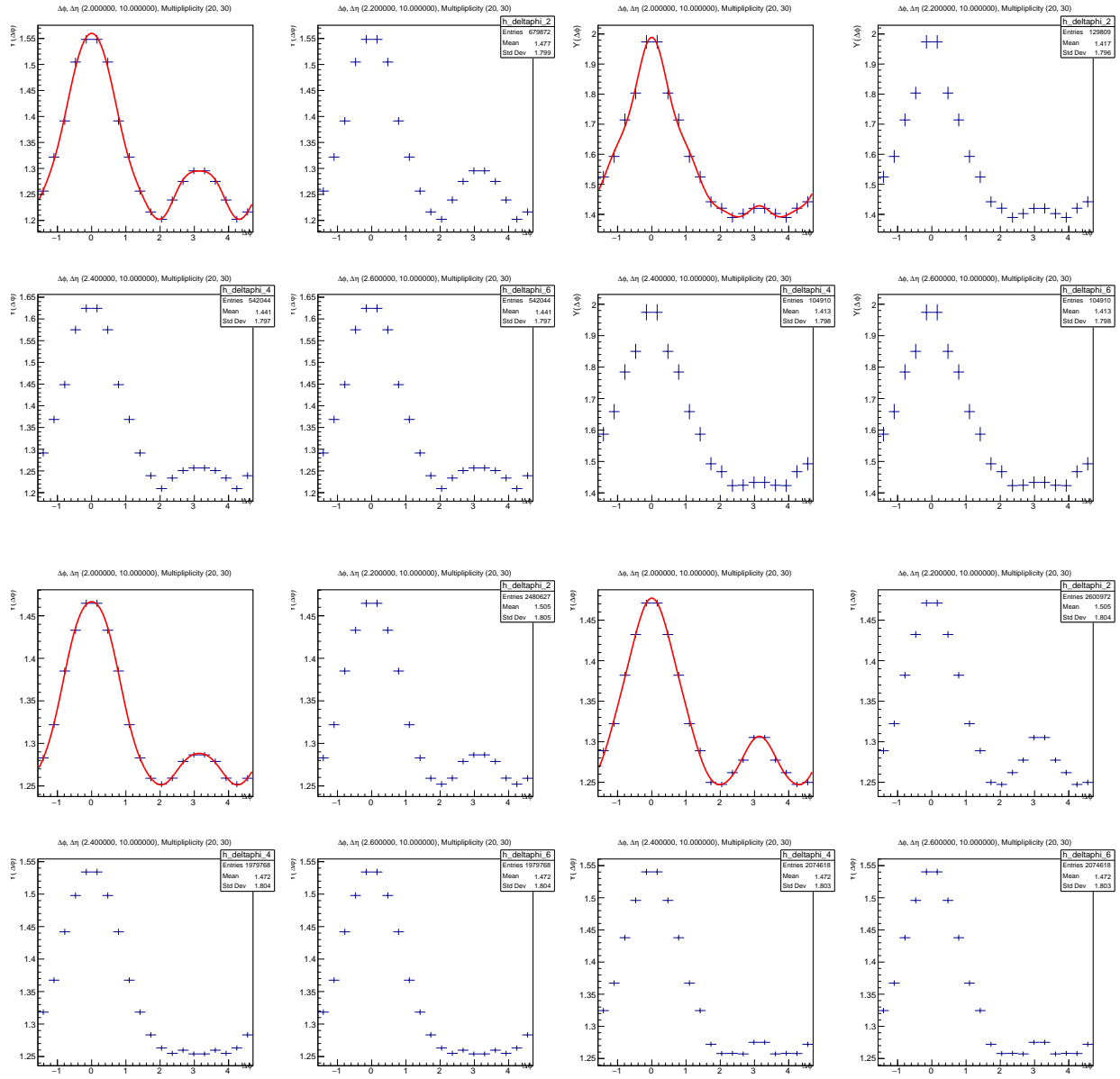


FIG. 58: Long range yield function for thrust axis. Top row is LEP1 and LEP2, bottom row PYTHIA8 and PYTHIA8 rope walk. Multiplicity 20-30.

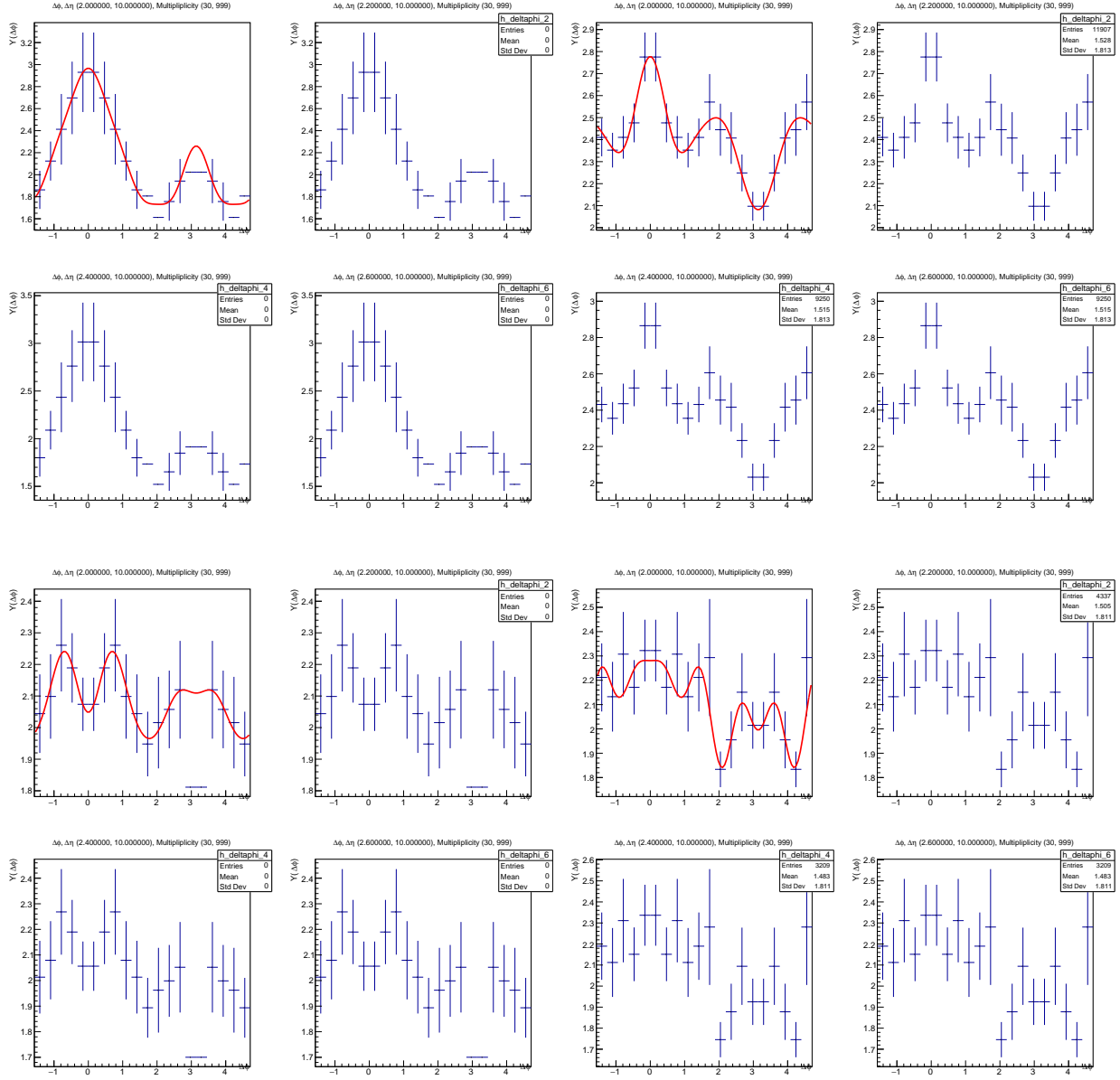


FIG. 59: Long range yield function for thrust axis. Top row is LEP1 and LEP2, bottom row PYTHIA8 and PYTHIA8 rope walk. Multiplicity 30-999.

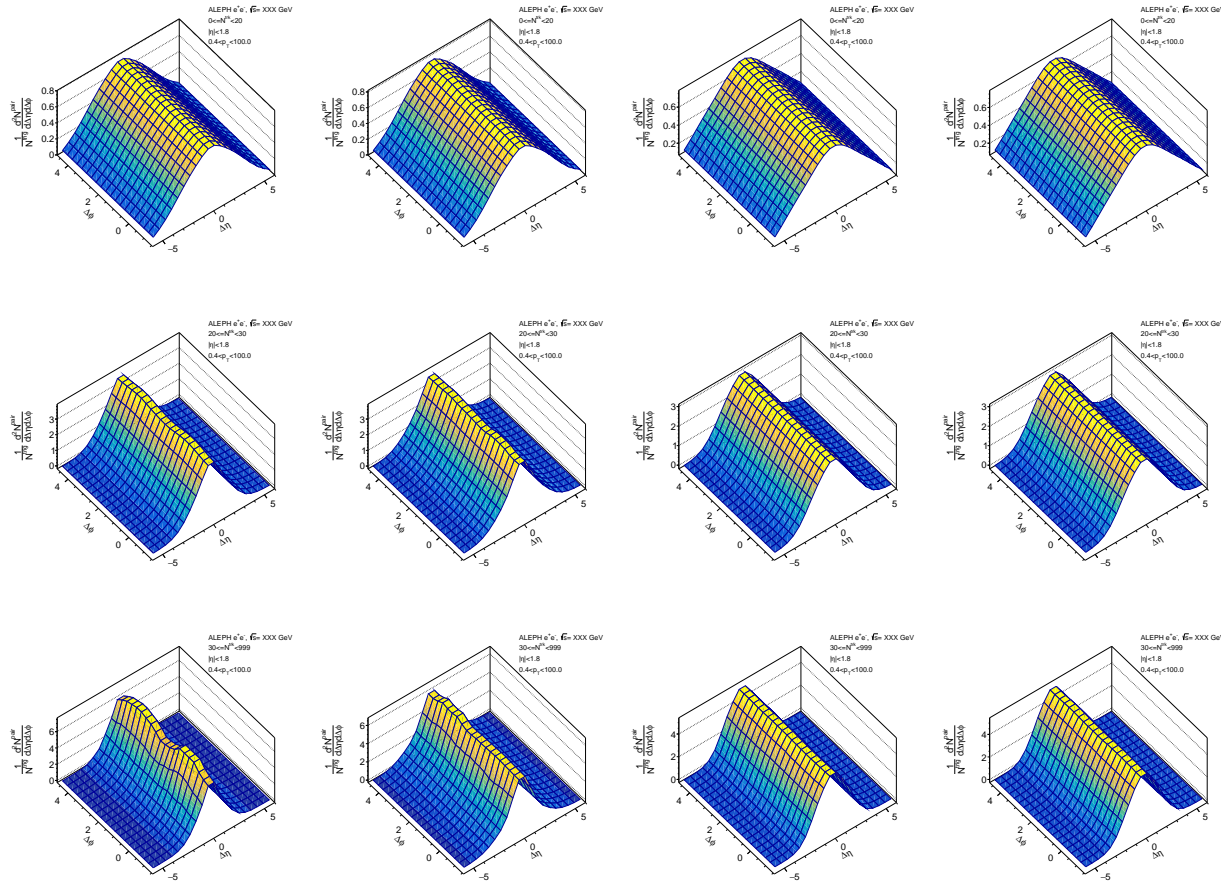


FIG. 60: Background function for WTA axis. Left to right: LEP1, LEP2, PYTHIA8, PYTHIA8 rope walk. Top to bottom: multiplicity 0-20, 20-30, 30-999.

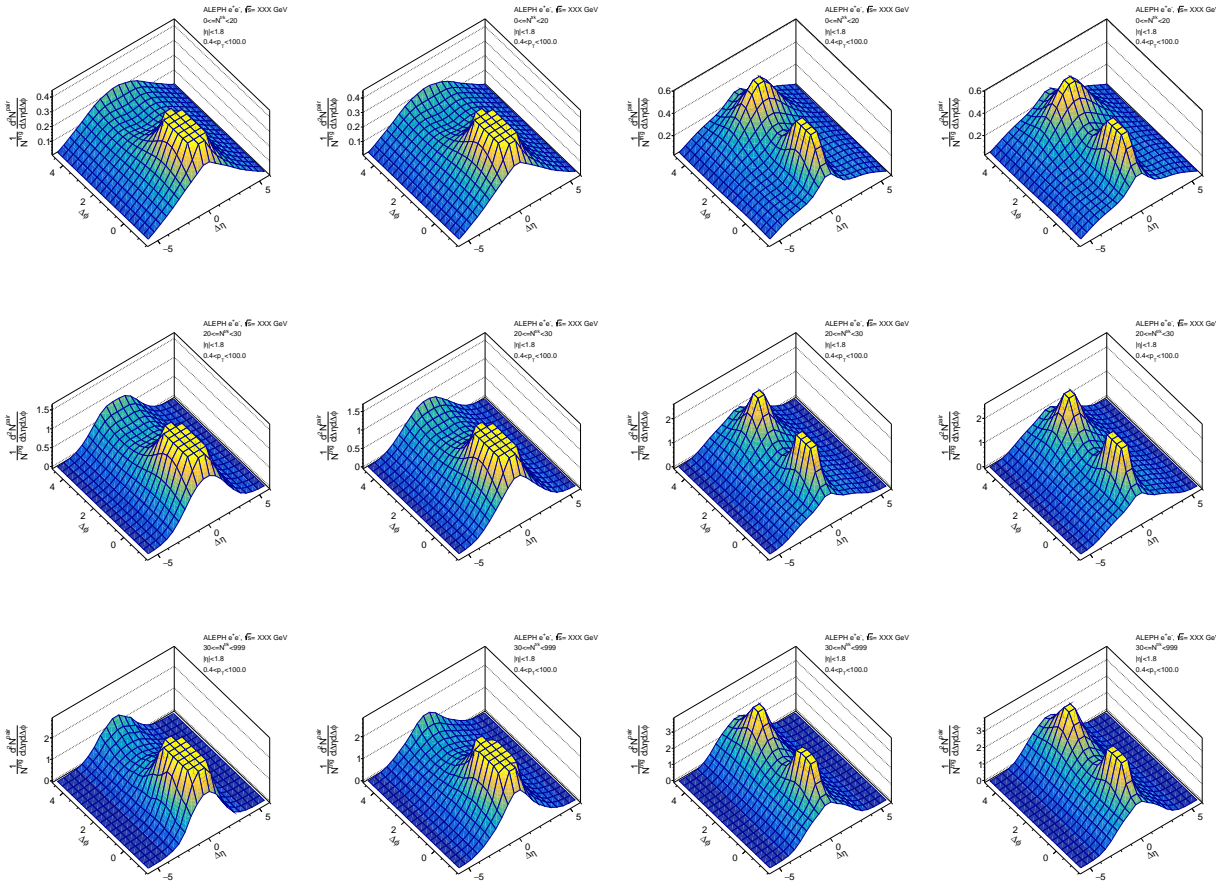


FIG. 61: Signal function for WTA axis. Left to right: LEP1, LEP2, PYTHIA8, PYTHIA8 rope walk. Top to bottom: multiplicity 0-20, 20-30, 30-999.

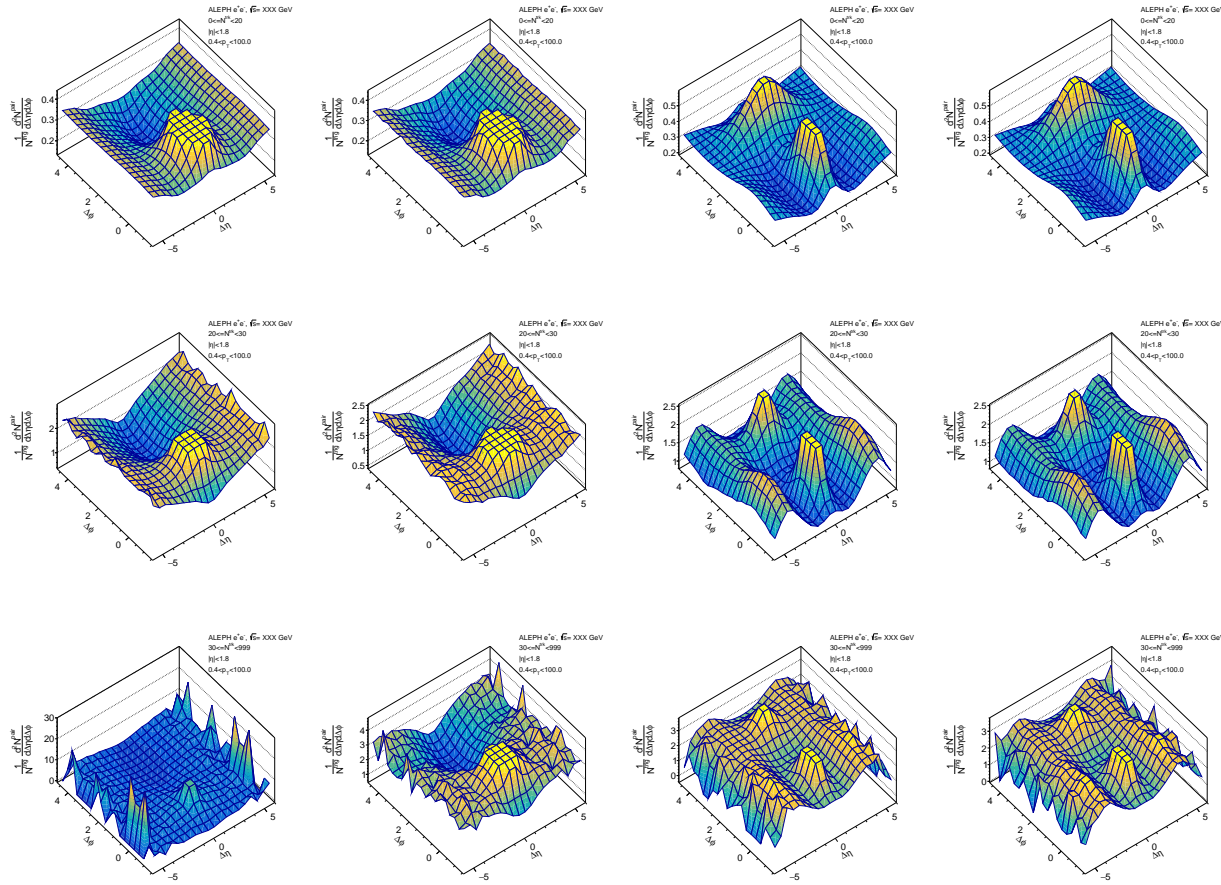


FIG. 62: Ratio function for WTA axis. Left to right: LEP1, LEP2, PYTHIA8, PYTHIA8 rope walk. Top to bottom: multiplicity 0-20, 20-30, 30-999. Note that the bottom left corner plot for LEP1 is zoomed out substantially from the plot to its right for LEP2 to show the difference in plotting that we may want to consider for the paper. The extremely high peaks at high $\Delta\eta$ and small $\Delta\phi$ are artifacts of the lack of a clear definition for the η cut in the WTA axis.

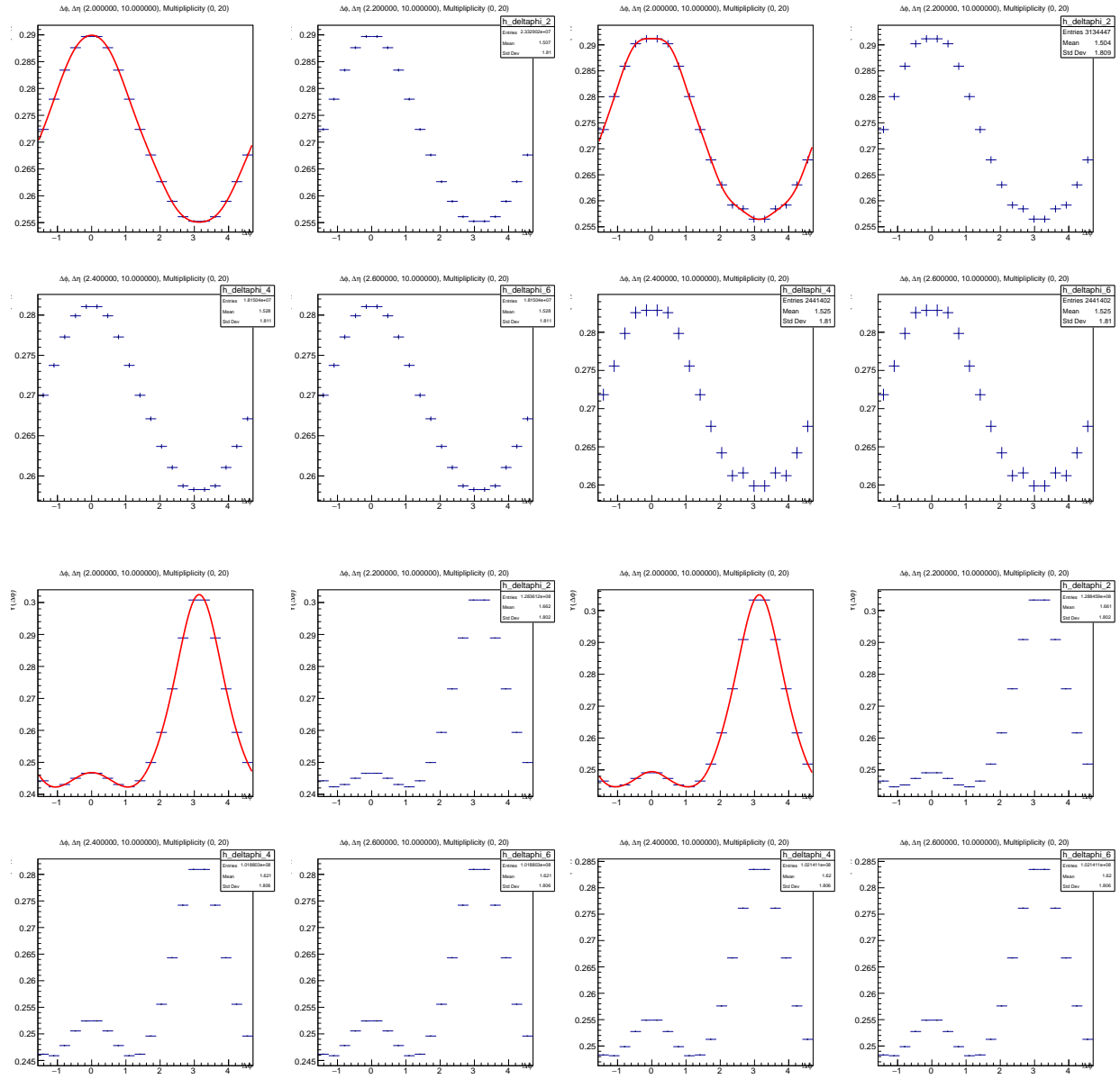


FIG. 63: Long range yield function for WTA axis. Top row is LEP1 and LEP2, bottom row PYTHIA8 and PYTHIA8 rope walk. Multiplicity 0-20.

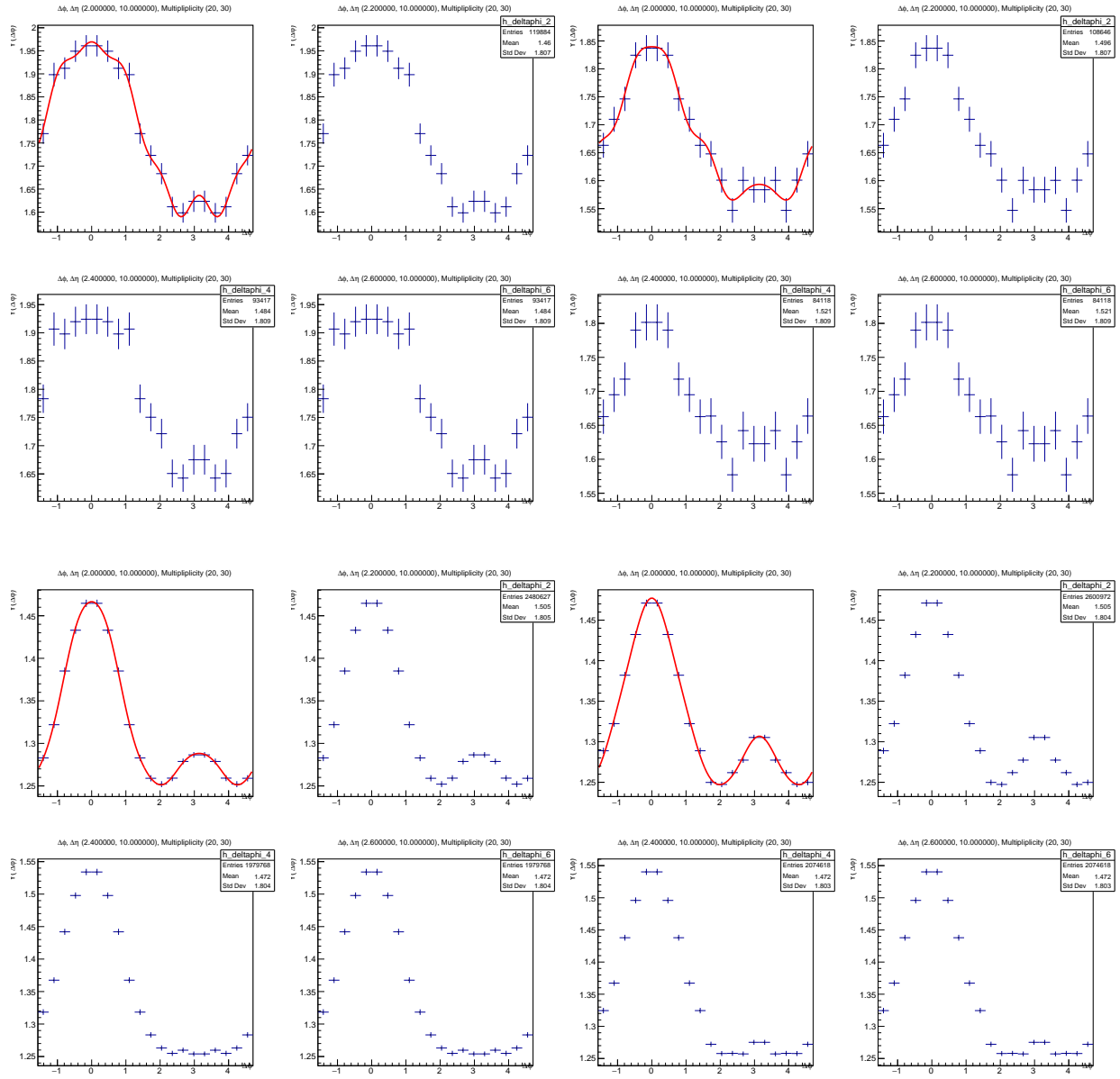


FIG. 64: Long range yield function for WTA axis. Top row is LEP1 and LEP2, bottom row PYTHIA8 and PYTHIA8 rope walk. Multiplicity 20-30.

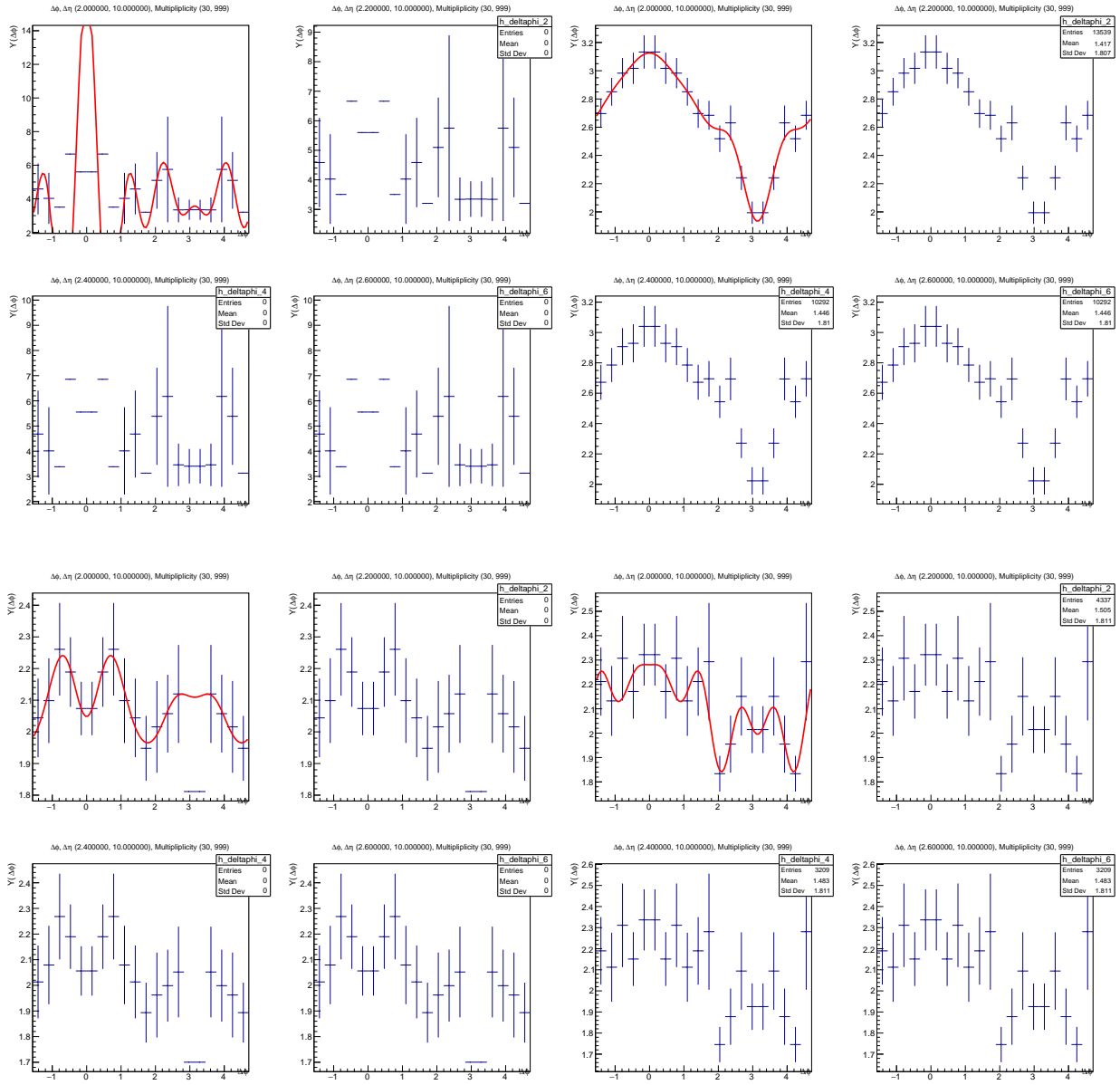


FIG. 65: Long range yield function for WTA axis. Top row is LEP1 and LEP2, bottom row PYTHIA8 and PYTHIA8 rope walk. Multiplicity 30-999.

B. Analysis for 2018.02.XX production

IX. SYSTEMATICAL UNCERTAINTIES

X. PRELIMINARY RESULTS FROM BELLE OPEN DATA

A. Charged hadron multiplicity distributions

Figure ?? shows the multiplicity distribution of identified hadrons (pions, kaons and protons) obtained after applying the selection on the particle transverse momentum ($0.1 < p_T < 4.0 \text{ GeV}/c$). The dominant contribution to the total event multiplicity is coming from pions as expected. In Fig. ??, the charged hadron multiplicity distribution N is shown. The multiplicity distribution is smooth and the largest raw particle multiplicity observed in these events is about 70 before corrections for tracking efficiency, misidentification and multiple reconstruction rates, which is large given the relatively low center-of-mass energy of the collisions. Detailed studies of primary vertex-track matching and track quality as well as possible pile-up event rejection are needed for the full Belle data analysis and those effects could lower the significance of the possible correlation signals.

FIG. 66: Uncorrected multiplicity distributions of pions (left), kaons (middle), protons (right) for particles in the range $0.1 < p_T < 4.0 \text{ GeV}/c$ in e^+e^- collisions.

FIG. 67: Multiplicity distribution of charged hadrons (protons, kaons and pions) for particles in the range $0.1 < p_T < 4.0 \text{ GeV}/c$ in e^+e^- collisions.

B. Two-particle correlation functions

In Fig. ??, the two-particle correlation functions from low ($N > 20$) and high multiplicity ($N > 50$) events are presented. In low-multiplicity events, the dominant features of the correlation function are the jet peak near $(\Delta\eta, \Delta\phi) = (0, 0)$ for pairs of particles originating

from the same jet and the elongated structure at $\Delta\phi \sim \pi$ for pairs of particles from back-to-back jets. The same-side jet peak and back-to-back correlation structures are also observed in high multiplicity events. In addition, a hint of “ridge”-like structure is visible at $\Delta\phi \sim 0$ in the right panel of Fig. ??.

To separate and inspect the long-range and short-range structure, one-dimensional distributions in $\Delta\phi$ are obtained by integrating over two $|\Delta\eta|$ intervals: $0 < |\Delta\eta| < 1$ and $2 < |\Delta\eta| < 3$. At small $\Delta\eta$, a near-side peak at $\Delta\phi = 0$ and the contribution from the back-to-back jet at $\Delta\phi = \pi$ is observed in the left panel of Fig ???. At large $\Delta\eta$, a near-side peak at $\Delta\phi = 0$ is shown in the right panel of Fig ???, similar to the structures observed in high multiplicity pp, pA and AA collisions over a wide range of energies. However, the significance of this signal is limited by the available statistics in the Belle open data. This motivates a detailed study with the high statistics hadronic data taken by the Belle collaboration.

FIG. 68: Two-particle correlation functions versus $\Delta\eta$ and $\Delta\phi$ in e^+e^- collisions for events with particle multiplicity > 20 (left) and > 50 (right).

FIG. 69: Two-particle correlation functions as a function of $\Delta\phi$ in e^+e^- in the pseudorapidity ranges $0 < \Delta\eta < 1$ (left) and $2 < \Delta\eta < 3$ (right) for events with particle multiplicity > 50 .

XI. SUMMARY

The ALEPH archived data has been used to perform measurements of two-particle angular correlation functions for the first time.

XII. APPENDIX

Cross check for two particle correlation plots. The cuts are specified in Table 1 and 2. The first column contains Anthony’s analysis, the second contains Austin’s cross-check, and the third contains the ratio of the two.

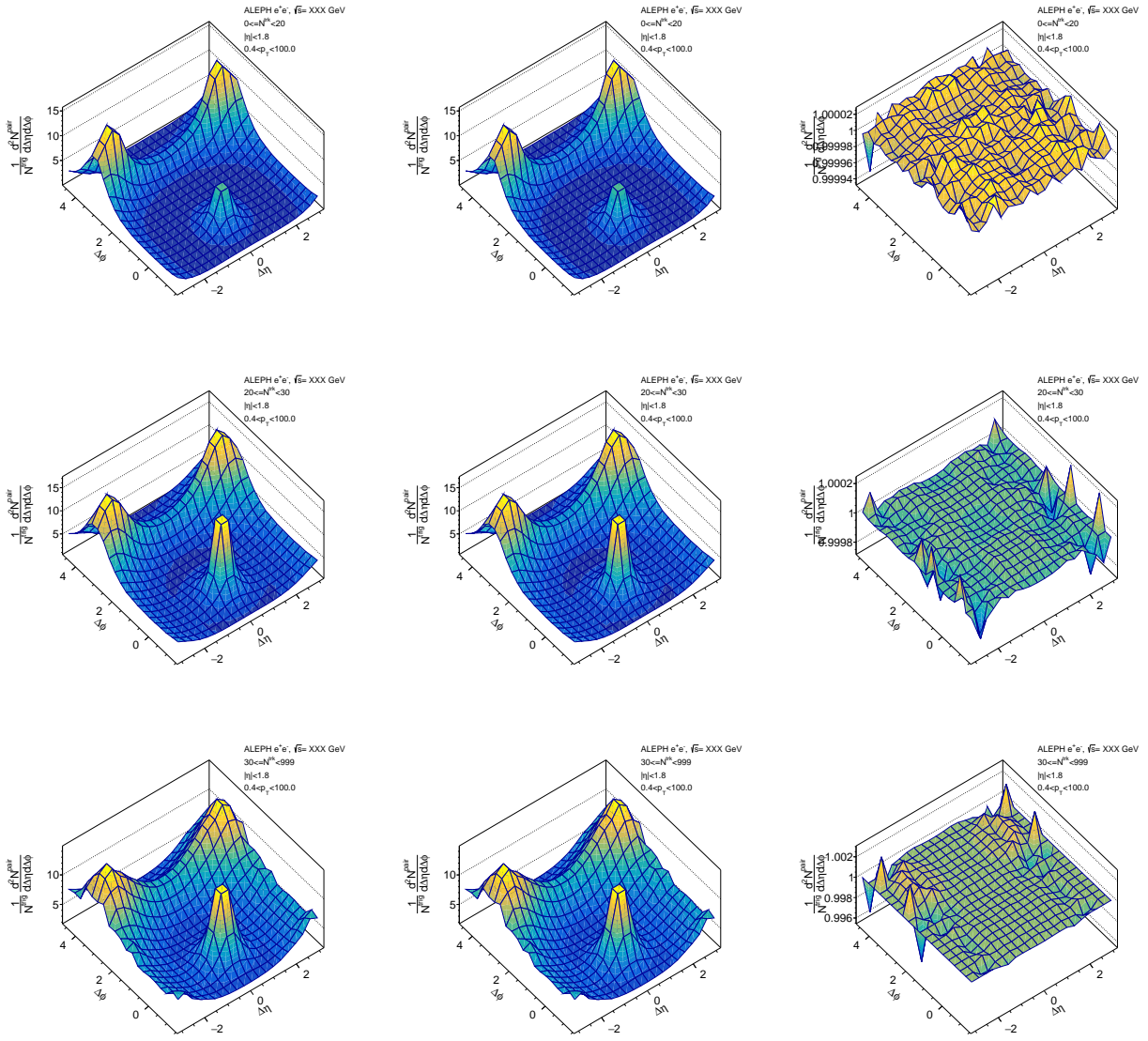


FIG. 70: Two particle correlation fuctions for the LEP1 data set analyzed in the beam axis.

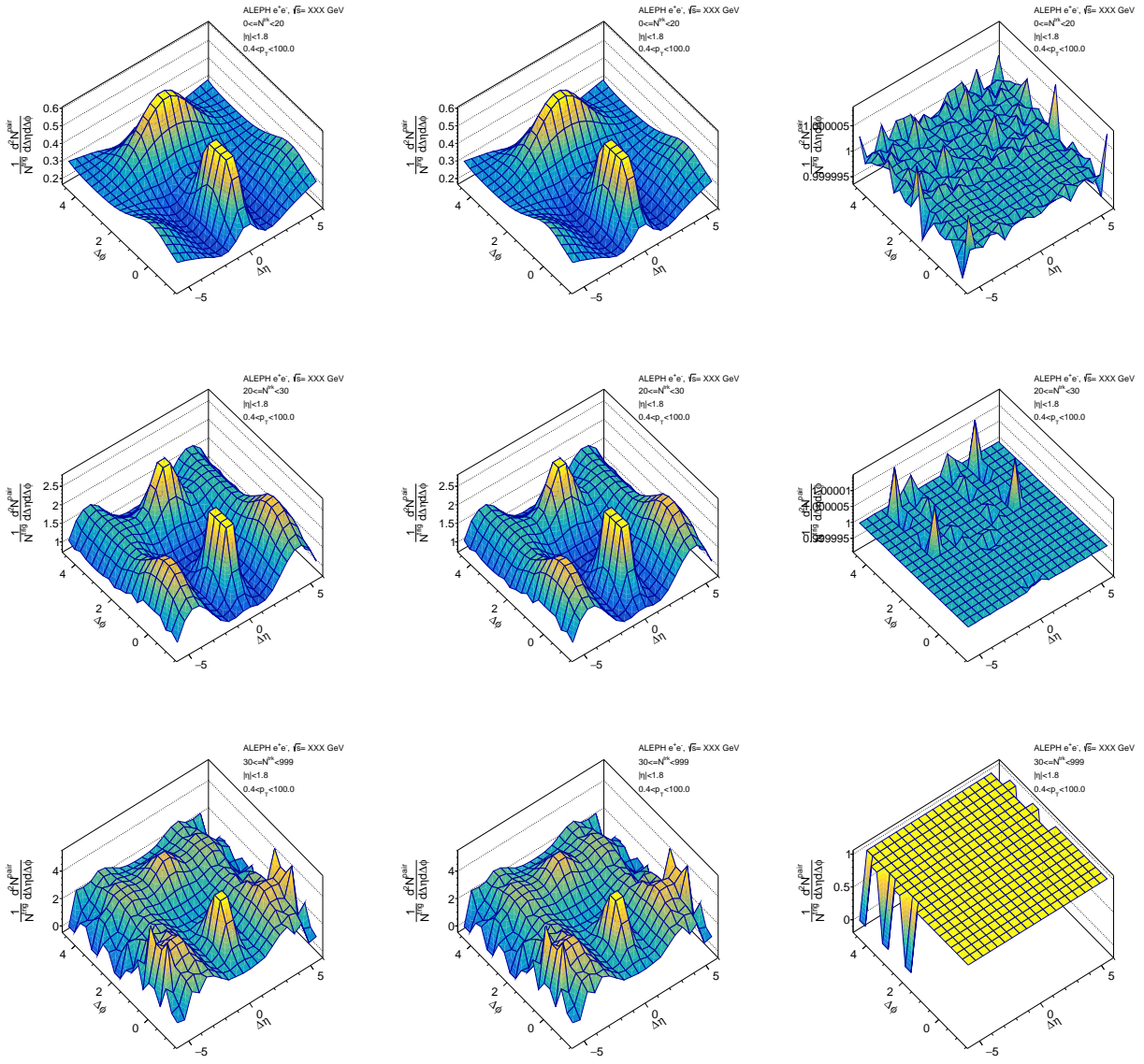
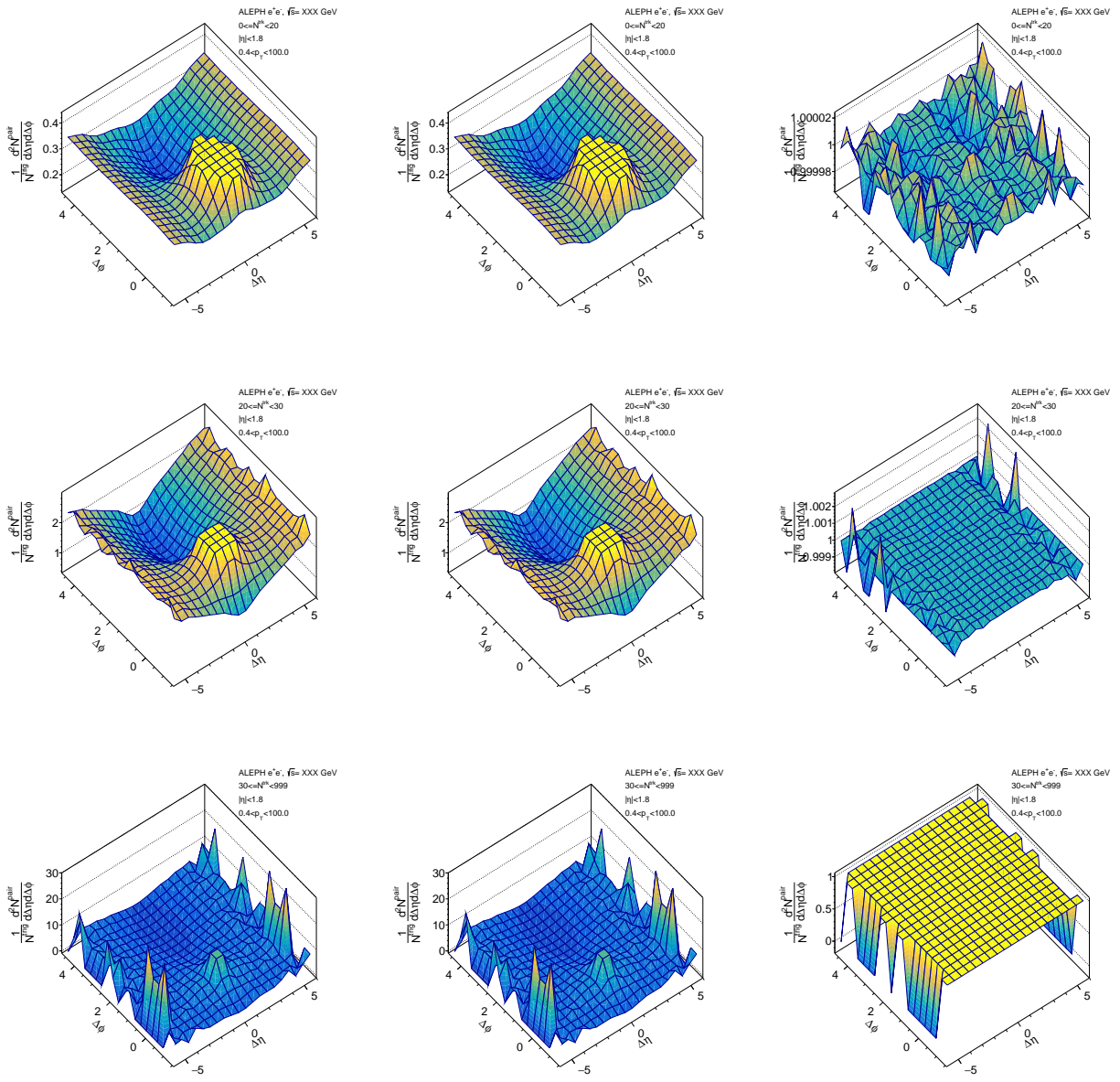


FIG. 71: Two particle correlation fuctions for the LEP1 data set analyzed in the thrust axis.



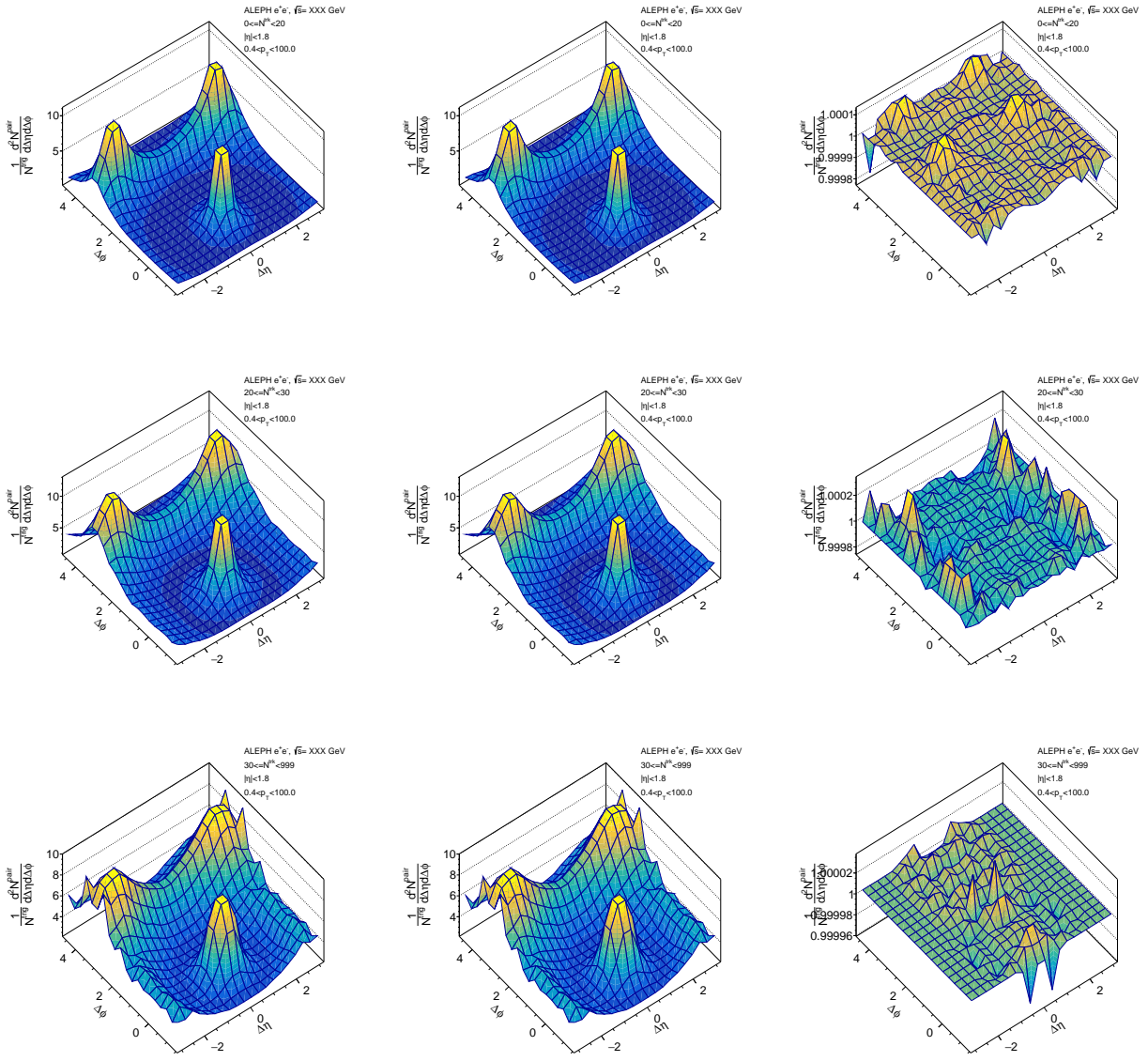


FIG. 73: Two particle correlation fuctions for the LEP2 data set analyzed in the beam axis.

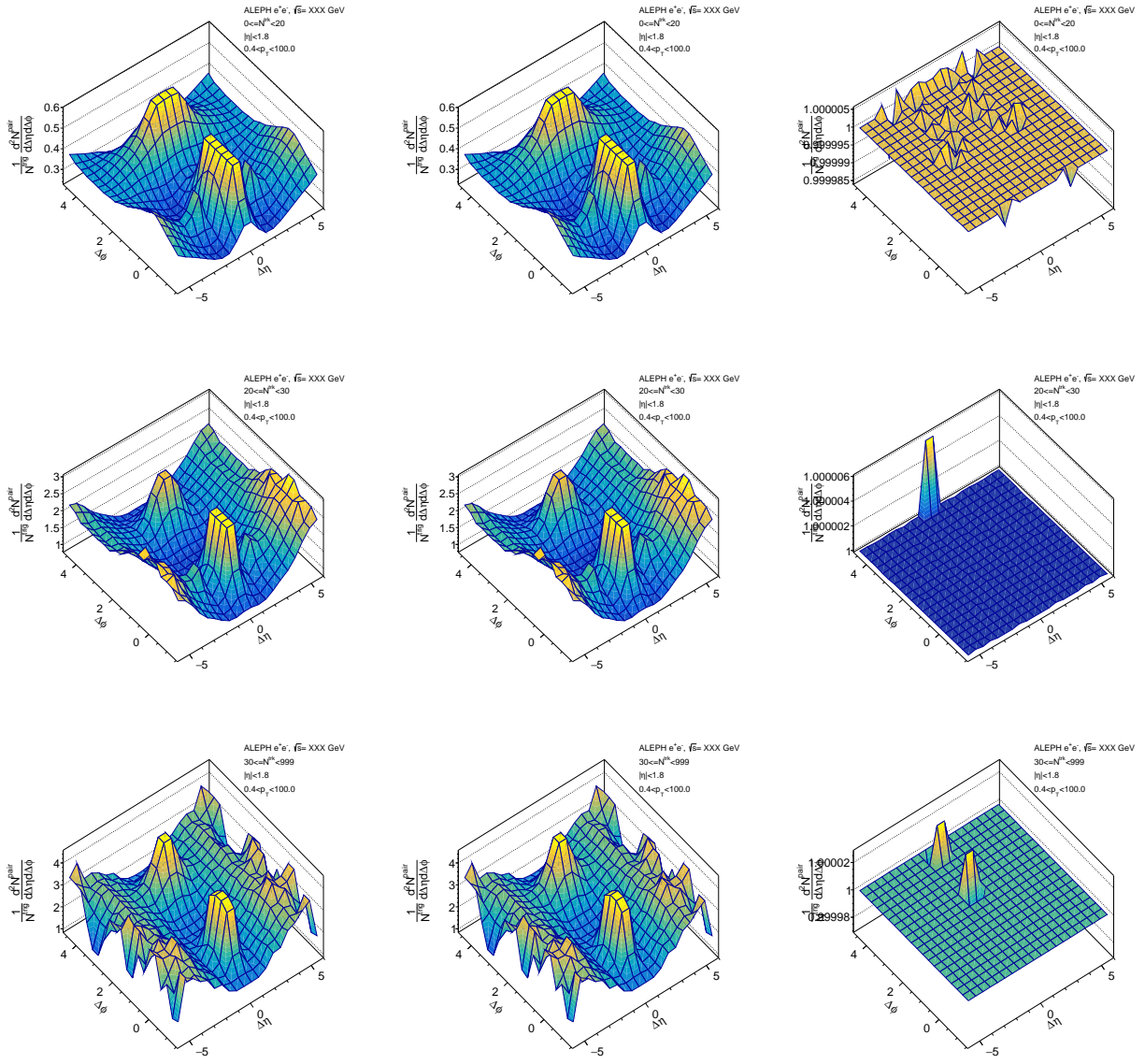


FIG. 74: Two particle correlation fuctions for the LEP2 data set analyzed in the thrust axis.

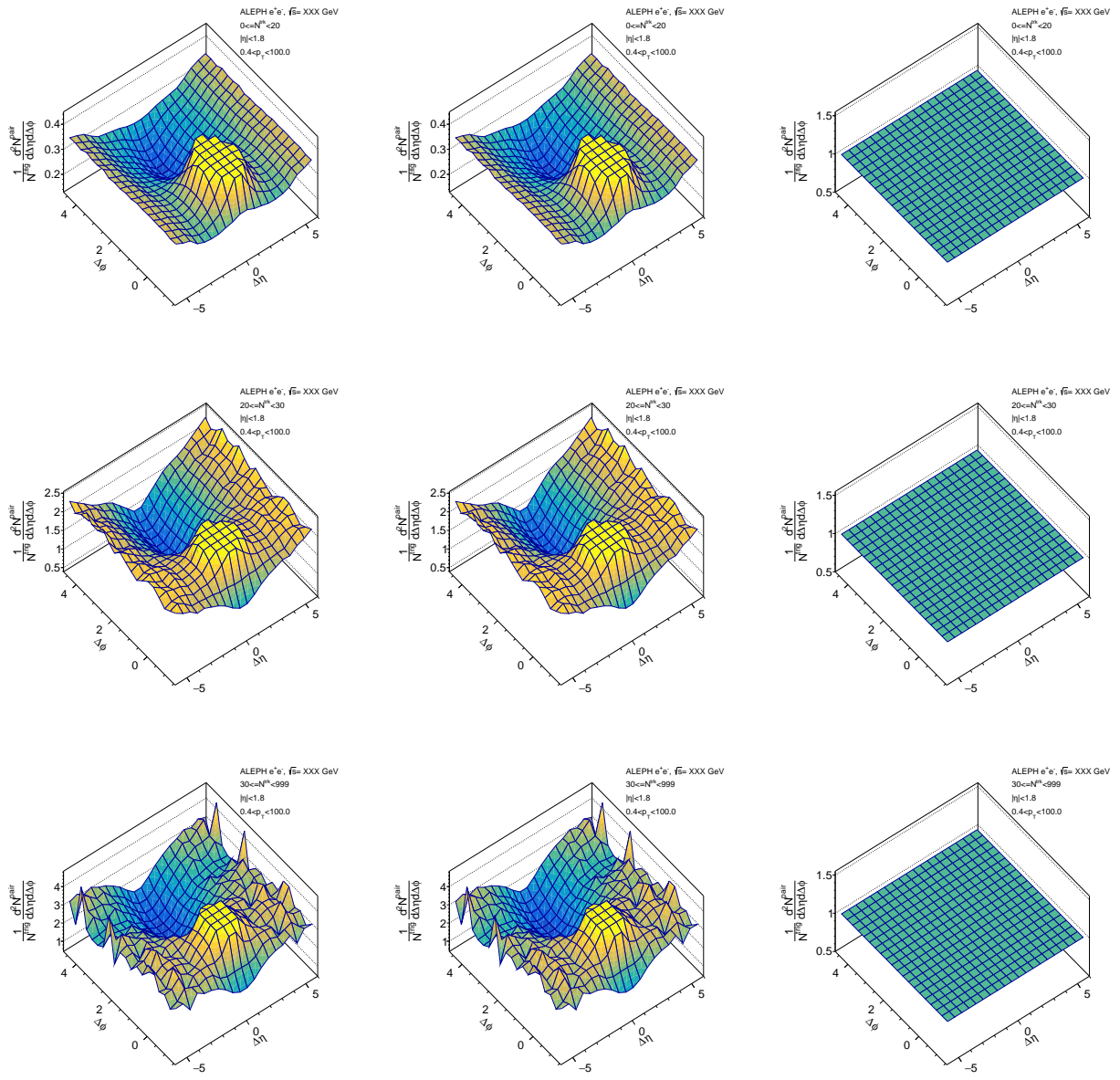


FIG. 75: Two particle correlation fuctions for the LEP2 data set analyzed in the WTA axis.

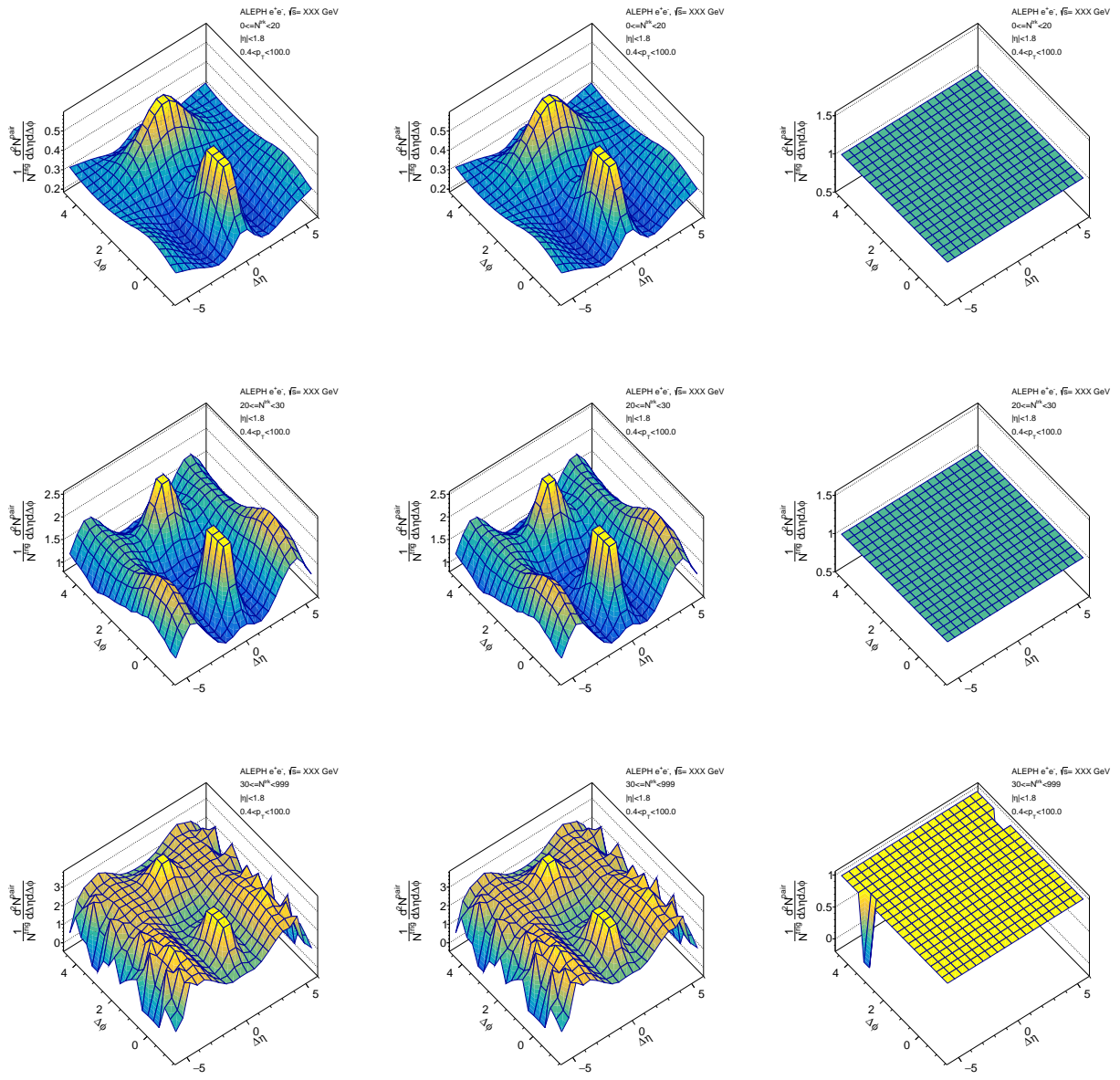


FIG. 76: Two particle correlation fuctions for the PYTHIA8 data set analyzed in the WTA axis.

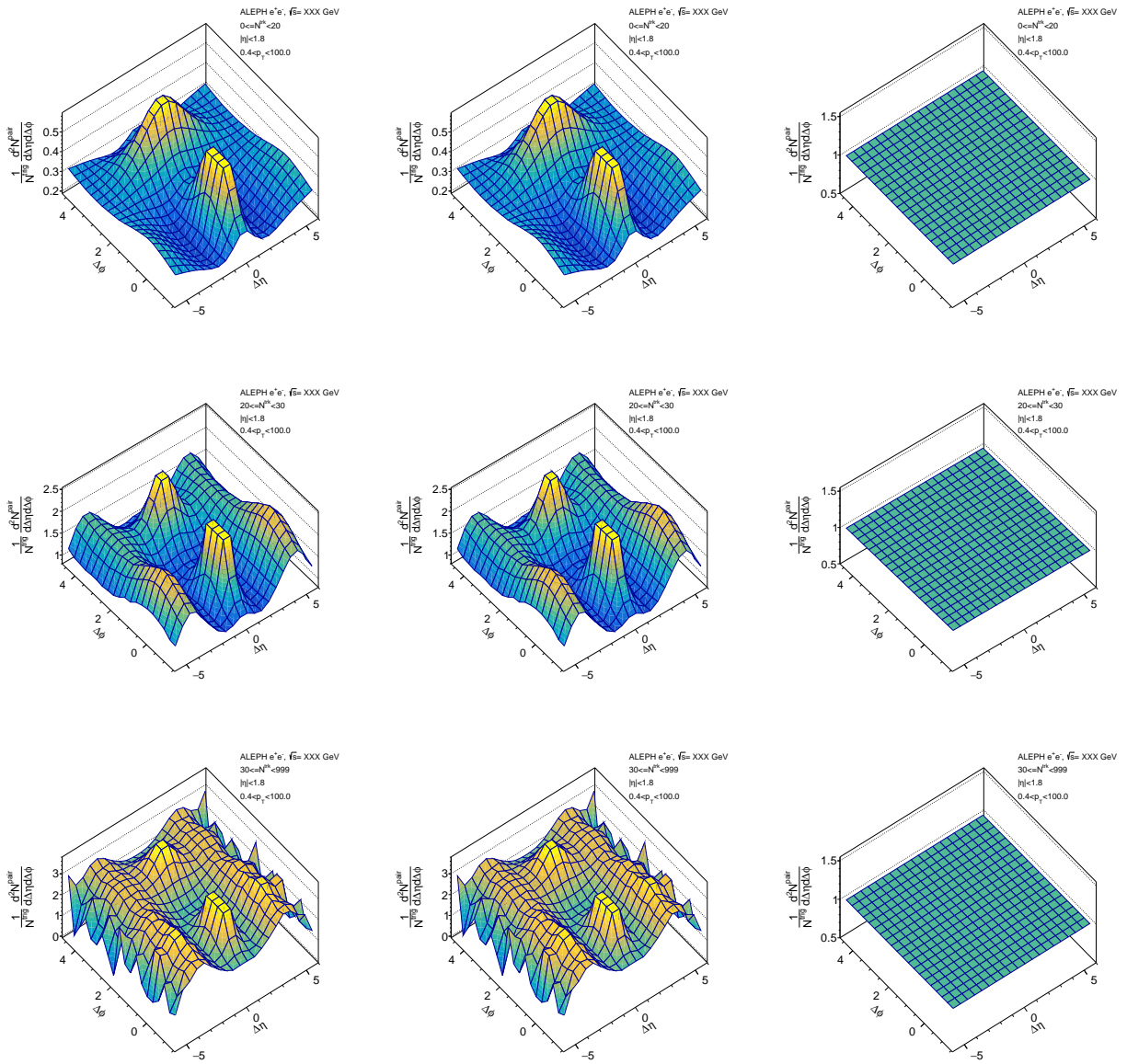


FIG. 77: Two particle correlation fuctions for the PYTHIA8 rope walk data set analyzed in the WTA axis.

-
- [1] CMS Collaboration, “Observation of Long-Range Near-Side Angular Correlations in Proton-Proton Collisions at the LHC”, *JHEP* **09** (2010) 091,
doi:10.1007/JHEP09(2010)091, arXiv:1009.4122.
- [2] CMS Collaboration, “Observation of long-range near-side angular correlations in proton-lead

- collisions at the LHC”, *Phys. Lett.* **B718** (2013) 795–814,
doi:10.1016/j.physletb.2012.11.025, [arXiv:1210.5482](https://arxiv.org/abs/1210.5482).
- [3] ALICE Collaboration, “Long-range angular correlations on the near and away side in p -Pb collisions at $\sqrt{s_{NN}} = 5.02$ TeV”, *Phys. Lett.* **B719** (2013) 29–41,
doi:10.1016/j.physletb.2013.01.012, [arXiv:1212.2001](https://arxiv.org/abs/1212.2001).
- [4] ATLAS Collaboration, “Observation of Associated Near-Side and Away-Side Long-Range Correlations in $\sqrt{s_{NN}}=5.02\text{TeV}$ Proton-Lead Collisions with the ATLAS Detector”, *Phys. Rev. Lett.* **110** (2013), no. 18, 182302, doi:10.1103/PhysRevLett.110.182302,
[arXiv:1212.5198](https://arxiv.org/abs/1212.5198).
- [5] ALICE Collaboration, “Elliptic flow of charged particles in Pb-Pb collisions at 2.76 TeV”, *Phys. Rev. Lett.* **105** (2010) 252302, doi:10.1103/PhysRevLett.105.252302,
[arXiv:1011.3914](https://arxiv.org/abs/1011.3914).
- [6] CMS Collaboration, “Centrality dependence of dihadron correlations and azimuthal anisotropy harmonics in PbPb collisions at $\sqrt{s_{NN}} = 2.76$ TeV”, *Eur. Phys. J.* **C72** (2012) 2012, doi:10.1140/epjc/s10052-012-2012-3, [arXiv:1201.3158](https://arxiv.org/abs/1201.3158).
- [7] B. B. Back et al., “The PHOBOS perspective on discoveries at RHIC”, *Nucl. Phys.* **A757** (2005) 28–101, doi:10.1016/j.nuclphysa.2005.03.084, [arXiv:nucl-ex/0410022](https://arxiv.org/abs/nucl-ex/0410022).
- [8] BRAHMS Collaboration, “Quark gluon plasma and color glass condensate at RHIC? The Perspective from the BRAHMS experiment”, *Nucl. Phys.* **A757** (2005) 1–27,
doi:10.1016/j.nuclphysa.2005.02.130, [arXiv:nucl-ex/0410020](https://arxiv.org/abs/nucl-ex/0410020).
- [9] PHENIX Collaboration, “Formation of dense partonic matter in relativistic nucleus-nucleus collisions at RHIC: Experimental evaluation by the PHENIX collaboration”, *Nucl. Phys.* **A757** (2005) 184–283, doi:10.1016/j.nuclphysa.2005.03.086, [arXiv:nucl-ex/0410003](https://arxiv.org/abs/nucl-ex/0410003).
- [10] STAR Collaboration, “Experimental and theoretical challenges in the search for the quark gluon plasma: The STAR Collaboration’s critical assessment of the evidence from RHIC collisions”, *Nucl. Phys.* **A757** (2005) 102–183, doi:10.1016/j.nuclphysa.2005.03.085,
[arXiv:nucl-ex/0501009](https://arxiv.org/abs/nucl-ex/0501009).
- [11] J.-Y. Ollitrault, “Anisotropy as a signature of transverse collective flow”, *Phys. Rev.* **D46** (1992) 229–245, doi:10.1103/PhysRevD.46.229.
- [12] B. Alver and G. Roland, “Collision geometry fluctuations and triangular flow in heavy-ion collisions”, *Phys. Rev.* **C81** (2010) 054905, doi:10.1103/PhysRevC.82.039903,

- 10.1103/PhysRevC.81.054905, [arXiv:1003.0194](#). [Erratum: Phys. Rev.C82,039903(2010)].
- [13] A. Bzdak, B. Schenke, P. Tribedy, and R. Venugopalan, “Initial state geometry and the role of hydrodynamics in proton-proton, proton-nucleus and deuteron-nucleus collisions”, *Phys. Rev.* **C87** (2013), no. 6, 064906, doi:10.1103/PhysRevC.87.064906, [arXiv:1304.3403](#).
- [14] K. Dusling, W. Li, and B. Schenke, “Novel collective phenomena in high-energy proton?proton and proton?nucleus collisions”, *Int. J. Mod. Phys.* **E25** (2016), no. 01, 1630002, doi:10.1142/S0218301316300022, [arXiv:1509.07939](#).
- [15] STAR Collaboration, “Inclusive charged hadron elliptic flow in Au + Au collisions at $\sqrt{s_{NN}} = 7.7 - 39$ GeV”, *Phys. Rev.* **C86** (2012) 054908, doi:10.1103/PhysRevC.86.054908, [arXiv:1206.5528](#).
- [16] F. Gelis, E. Iancu, J. Jalilian-Marian, and R. Venugopalan, “The Color Glass Condensate”, *Ann. Rev. Nucl. Part. Sci.* **60** (2010) 463–489, doi:10.1146/annurev.nucl.010909.083629, [arXiv:1002.0333](#).
- [17] K. Dusling and R. Venugopalan, “Comparison of the color glass condensate to dihadron correlations in proton-proton and proton-nucleus collisions”, *Phys. Rev.* **D87** (2013), no. 9, 094034, doi:10.1103/PhysRevD.87.094034, [arXiv:1302.7018](#).